Deciphering landscape evolution with karstic networks: A Pyrenean case study

Amandine Sartégou, Didier L. Bourlès, Pierre-Henri Blard, Regis Braucher,
Bouchaib Tibari, Laurent Zimmermann, Laëtitia Leanni, Georges Aumaitre,
Karim Keddadouche

Deciphering landscape evolution with karstic networks: A Pyrenean case study

Amandine Sartégou *(1,2), Didier L. Bourlès (2), Pierre-Henri Blard (3), Régis Braucher (2), Bouchaib Tibari (3), Laurent Zimmermann (3), Laëtitia Leanni (2), and ASTER Team[+] (2)

(1) Université de Perpignan–Via Domitia, CNRS UMR 7194 Histoire Naturelle de l'Homme Préhistorique, 52 avenue Paul Alduy, F-66860 Perpignan Cedex, France ; (2) Aix-Marseille Université, CNRS-IRD-Collège de France, UM 34 CEREGE, Technopôle de l'Environnement Arbois-Méditerranée, BP80, 13545 Aix-en-Provence, France ; (3) CRPG, UMR 7358, CNRS-Université de Lorraine, 15 rue Notre-Dame des Pauvres, 54501 Vandœuvre-lès-Nancy, France

[+] Georges Aumaître, Karim Keddadouche

*corresponding author at: Université de Perpignan – Via Domitia, UMR 7194 CNRS, 52 avenue Paul Alduy, 66860 Perpignan, France.

E-mail address: amandine.sartegou@univ-perp.fr (A. Sartégou).

Abstract

The rates and chronologies of valley incision are closely modulated by the tectonic uplift of active mountain ranges and were controlled by repeated climate changes during the Quaternary. The continental collision between the Iberian and Eurasian plates induced a double-vergence orogen, the Pyrenees, which has been considered a mature mountain range despite significant seismicity and evidence of neotectonics. Nevertheless, recent studies indicated that the range may have never reached a steady state. One option for resolving this controversy is to quantify the incision rates since the Miocene by reconstructing the vertical movement of geometric markers such as fluvial terraces. However, the few available ages for the Pyrenean terrace systems do not exceed the Middle Pleistocene. Thus, we study alluvium-filled horizontal epiphreatic passages in limestone karstic networks to increase the span of this dataset. Such landforms are used as substitutes of fluvial terraces because they represent former valley floors. These features record the transient position of former local base levels during the process of valley deepening. The Têt river valley (southern Pyrenees) is studied near the Villefranche-de-Conflent limestone gorge, where 8 cave levels have been recognized over a vertical height of 600 m. In this setting, already published $^{26}Al/^{10}Be$ cosmogenic burial data were limited to the last ~5 Ma. This work extends this initial dataset through the acquisition of cosmogenic $^{10}Be/^{21}Ne$ data, which should enable us to reconstruct a more

complete valley incision chronology. We also revise the ^{26}Al/^{10}Be record for the lowest portion of the valley. The obtained quantitative results are surprising relative to certain geological evidence, and the limitations of such an approach in the investigated geodynamic context are discussed. In particular, sampling within a detrital deposit (the Escaro Formation) and in the riverbeds suggests that the ^{26}Al/^{10}Be ratios that are associated with the lower cave levels could have been inherited by pre-burial episodes. Similarly, pre-burial catchment denudation rates that do not exceed hundreds of cm/ka are probably tainted by the same amalgamation processes.

Keywords

Cave deposits, cosmogenic burial dating, ^{26}Al, ^{10}Be, ^{21}Ne, incision rates, Pyrenees.

Highlights

- Exceptional preservation of a Neogene canyon in the eastern Pyrenees is observed, with 8 epiphreatic cave levels
- ^{26}Al/^{10}Be and ^{10}Be/^{21}Ne burial durations are obtained for intrakarstic alluvial deposits in 8 cave levels
- The post-Messinian inferred incision rates and the ^{10}Be-derived denudation rates cannot be used as proxies for quantifying landscape development because of possible amalgamation processes
- The results indicate valley incision since the Burdigalian with possible pronounced fluctuations since the Messinian

1. Introduction

The formation and evolution of a mountain range are considered to result from both internal (tectonics) and external (climate) forcing. Numerous authors attempted to demonstrate that the climate would have a major influence on the dynamics of this antagonism at various spatial and/or temporal scales (e.g., Molnar et England, 1990; Reiners et al., 2003; Whipple et al., 2009), although this primary control is still ardently discussed (e.g., Godard et al., 2014). However, highlighting the retroactive interactions between these two forces is as complicated as comparing phenomena that occur on variable timescales. A key point to better constrain the formation and evolution of mountain ranges is to determine the distribution of the deformation and its temporal evolution. The Pyrenees, which have preserved distinct Mesozoic and Cenozoic geodynamic environments, are a unique mountain

70 range within European orogens. However, our understanding of the recent geodynamic

71 evolution of this chain remains quite fragmentary. Researchers have identified an initial phase

72 of orogeny between ~84 Ma and ~65 Ma, followed by a potential quiescence phase up to 59

73 Ma long that predated a recovery in orogenesis (Ford et al., 2015). Furthermore, the eastern

74 section of the chain could never have reached a steady state. Despite the improvement in

75 observational techniques over the past decade and the acquisition of numerous

76 thermochronological data (e.g., Fitzgerald *et al*., 1999, Maurel et al., 2008, Vacherat et al,

77 2016), supplementary data are still required to constrain the recent evolution (last 20 Ma) of

78 the chain. As an example, the origin of the flat surfaces at high altitudes (e.g., Babault et al.,

79 2005; Calvet and Gunnell, 2008; Bosch et al., 2016; see Supp. Info) and their significance

80 with regard to a potential post-orogenic uprising is still debated, these paleo-surfaces being

81 (deeply) incised (e.g., Ortuño et al., 2013; Monod et al., 2016; Mouchené et al., 2017).

82 Another critical point is the high microseismicity of the chain, which is quite incompatible

83 with a moderate potential activity (e.g., Chevrot et al., 2011). In addition, recent work on the

84 Lannemezan mega-cone showed that intense Mio-Pliocene tectonic activity is not required to

85 form this mega-structure (Mouchené et al., 2017).

86   One option for resolving this controversy is to quantify the incision rates since the

87 Miocene by reconstructing the vertical movement of geometric markers, such as fluvial

88 terraces. However, the few available ages for the Pyrenean terrace systems do not exceed the

89 end of the Lower Pleistocene (e.g., Stange et al., 2013; Delmas et al., 2015). Moreover,

90 alluvial terraces are poorly preserved in some valleys. Thus, we study alluvium-filled

91 horizontal epiphreatic passages in limestone karstic networks to increase the time span of this

92 dataset. Such landforms are used as substitutes of fluvial terraces because they represent

93 former valley floors (e.g., Palmer, 2007; Audra et al., 2013). These features record the

94 transient position of former local base levels during the process of valley deepening. Until

95 now, only relative dating based on correlations between staged levels and external terraces

96 have been conducted on caves in the study area. However, establishing the absolute

97 chronology of a cave's genesis remains rather complex, even if the absolute dating of the

98 trapping of alluvium in caves with the cosmogenic burial dating method may be relevant in

99 this case (e.g., Granger et al, 1997; Häuselmann et al., 2005; Tassy et al., 2013). The classical

100 cosmogenic nuclide chronometer for this task is the combination of in situ-produced ^{26}Al and

101 ^{10}Be cosmogenic nuclides that are measured in quartz, which cover the 0.2-6 Ma period. A

102 preliminary study of two stepped systems in the Têt river valley was led by Calvet et al.

103 (2015). The obtained burial durations yielded a mean incision rate of ~55 m/Ma since the

104 Zanclean (5.3 – 3.6 Ma), which increased to 92 m/Ma during the Quaternary. These authors

105 also established that pre-burial catchment denudation rates ranged from 35 to 7 m/Ma, with an

increase during the Early Quaternary. Nevertheless, this method has several limitations: notably, the ^{26}Al-^{10}Be couple cannot be used to date objects older than 6 Ma because of their respective half-lives (^{26}Al: (0.717±0.024) Ma; ^{10}Be: (1.387±0.012) Ma) alongside the sensitivity of the accelerator mass spectrometry technique. To overcome this limitation, one solution involves analyzing the concentration in the stable nuclide ^{21}Ne within the same mineral to obtain the ^{21}Ne-^{10}Be burial durations (e.g., Balco and Shuster, 2009; McPhilipps et al., 2016).

Considering the promising results from this initial study (Calvet et al., 2015), we decided to complete the dataset and densify the sampling in the already studied cavities. For this purpose, eight levels in the Têt river catchment, which is one of the easternmost valleys of the Pyrenees, were explored. We surveyed fifteen horizontal caves and collected alluvial deposits in eleven of them to measure their cosmogenic nuclide concentrations (^{10}Be, ^{26}Al and/or ^{21}Ne). We also re-analyzed the samples that were measured by Calvet et al. (2015) and additional samples from the same caves. The quantitative data that were acquired and presented in this paper reveal inconsistencies with some of the geological observations, so the methodology will be questioned through the investigation of potential non-visible effects, such as particle sizes and lithology disparities. The basic methodology, including the need to consider that the burial durations and/or paleo-denudation rates are calculated from TCN concentrations averaged from an amalgams of quartz grains taken from sedimentary deposits, is also questioned. Methodological cross-checking between the ^{21}Ne-^{10}Be and ^{26}Al-^{10}Be cosmogenic pairs have thus been conducted when possible for a better understanding of the related impacts of these parameters. Finally, the obtained scattered paleo-denudation rates and the limitations of such an approach in the Pyrenean geodynamic context are discussed.

2. Geological and geodynamical contexts

2.1. Lithological and structural contexts of the eastern Pyrenees

The Pyrenees are a mountain range in southwestern Europe. This mountain range, which forms a 400 km-long geographical barrier of N110°-orientation and had developed along the boundary between the Iberia and European plates (Choukroune, 1992), is the result of the Late Cretaceous–Cenozoic inversion of a Cretaceous transcurrent hyper-extended rift that was created during the opening of the Bay of Biscay (Lagabrielle et al., 2010). The structures continue along the southern shore of the Bay of Biscay to the Asturias to the west, which extends this chain to 600 km.

The axial zone of the Pyrenees consists of various terrains of Precambrian and Paleozoic ages, which were folded during the Hercynian orogeny in the Carboniferous (355-

295 Ma; Engel, 1984). The studied catchment area (Figure 1) includes the Puigmal-Canigou, Carlit and Madrès massifs. The axis of the Madrès massif consists of the WNW-ESE syncline of Villefranche-de-Conflent (Guitard et al., 1998), which is a stack of Hercynian late-folded syncline foliage that affected the sedimentary or slightly metamorphosed formations from the Middle and Upper Paleozoic. The base of the valley has massive outcrops of Devonian and Carboniferous limestones and dolomites. Towards the top of the stratigraphic series (Silurian - Upper Ordovician and Lower Carboniferous - Visean), pelites, calcschists, argillites and sandstone schists, which are generally less resistant to erosion because of their laminated structure, are predominant. Two thick sets of Ordovician, Cambrian and probably Precambrian schistose rocks flank this axis. These various petrographic formations (pelitic, schistous, marble, microconglomeratic and volcanodetritic facies) form the Canaveilles (Laumonier et al., 1996, 2015) and Jujols series from the base to the summit (Laumonier et al., 1996, 2015). These rocks are intruded by Ordovician granite plutons.
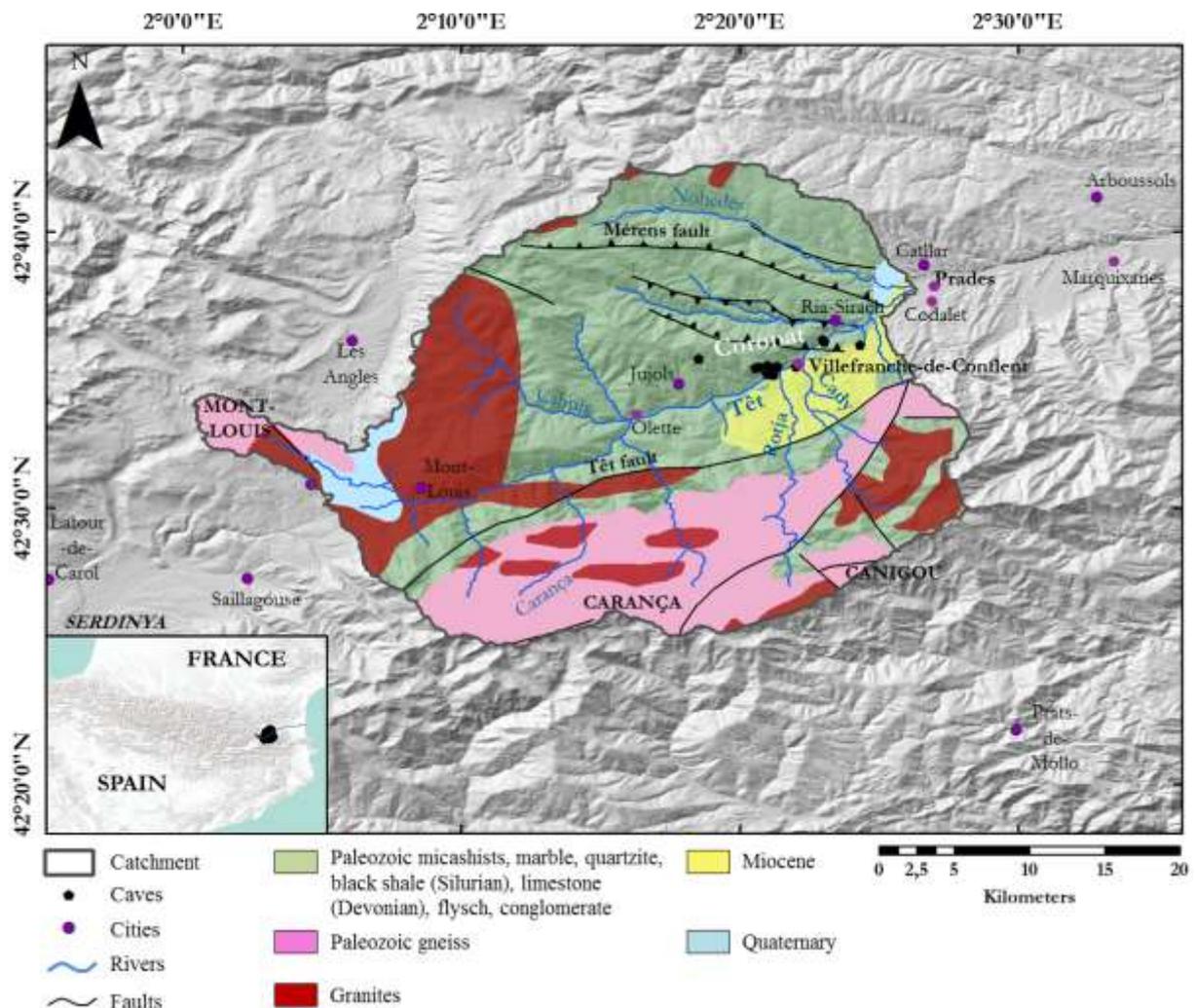
Figure 1 : Lithostructural features of the Têt catchment (according to IGME – BRGM data). Alluvial sediments that were trapped in karstic networks originated from Paleozoic crystalline massifs (gneiss, granites), metasediments and supposed Miocene deposits from the Escaro Formation because of the

159   Miocene extension phase. The watershed also includes glacial deposits at high altitudes. For a more

160   detailed map of the studied area, refer to Calvet et al. (2015).

161   Around 20-25 Ma ago, collision-related deformation in the central and eastern

162   Pyrenees ceased, the crustal deformation resulting from the convergence between the Iberia

163   and European plates being then accommodated by the Betic Cordillera (Vergés et al., 2002).

164   After the collision or during the last phase of plate convergence, while the central and western

165   Pyrenees remained under a compressive regime, the eastern Pyrenees were affected by a

166   period of crustal thinning that was related to the well-defined Oligocene–Early Miocene

167   rifting that affected the Gulf of Lions (e.g., Ortuño et al., 2013). During the Lower Miocene

168   (21-15 Ma), the eastern Pyrenean domain collapsed and was then divided into grabens that

169   were filled with thick detrital sedimentary series (Guitard et al., 1998 and references therein).

170   These features in the Roussillon and Conflent basins, the Escaro and Col de Fins formations,

171   are estimated to have been deposited during the Lower Miocene (Figure 1; Supp. Info). These

172   are fluviatile formations, composed of clasts coming from the Têt River high valley and the

173   surrounding massifs such as the Canigou massif. This succession of collapse events followed

174   by filling phases towards the Early Miocene has sometimes been called into question.

175   Then, the closure of the strait between the Atlantic Ocean and the Mediterranean Sea

176   at the end of the Miocene (~5.9 Ma; Gautier et al., 1994; Suc et al., 1994) leaded to a drop of

177   1500 m of the base level (Hsü et al., 1973) which broke the eustatic equilibrium. This event,

178   called the Messinian Salinity Crisis (MSC), induced a major incision of the peri-

179   Mediterranean pre-MSC drainage systems (e.g., Hsü et al., 1973; Clauzon, 1982). Very deep

180   canyons were then dug. Some vestiges of Pliocene detrital deposits filling these canyons (e.g.

181   Depéret, 1895) as well as the upstream propagation of the incision, depicted by knickpoint

182   migration, have been studied (e.g., Loget and Van Den Driessche, 2009). The morphology of

183   the canyons is *a priori* indeed well preserved because of the sudden rise of the base level (+80

184   m from the current level) and of the concomitant deposition of sediments in Gilbert deltas

185   which reduced the rivers erosive power (e.g., Clauzon et al., 1995; Loget et al., 2006).

186   Opinions differ as to whether the Têt River valley, particularly the Conflent area, is a

187   Messinian paleo-canyon. The history of the Upper Miocene and of the Messinian evolution of

188   the Conflent Basin is still debated. It is currently accepted that deposits of the late Miocene,

189   the Col de Fins Formation, which is consisting of fluvial facies and quartzite blocks, would be

190   present west of the basin. This deposit would have been largely denuded in response to the

191   MSC, leaving only a few scraps.

192   The Lower Pliocene formations of and near the area consist of marine clay, while the

193   Upper Pliocene formations are dominated by fluvial arkosic sands and conglomerates. These

194   detrital sedimentary series were partially removed and remobilized by river downcutting

195   during the Upper Pliocene and Pleistocene. Staircased alluvial terraces that range from 20 to

196   200 m above the present-day thalweg support this incision. Based on current weathering

197   profiles (Calvet, 1996), cartographic relationships (Delcaillau et al., 2004), and heavy mineral

198   contents (Debals, 2000), the chronology of this fluvial downcutting still requires absolute

199   dating to be better constrained. In this area, the Quaternary superficial formations are

200   represented by the high terraces to the SE of Ria (Calvet et al., 2015). The lower terraces

201   occupy a large portion of the Têt valley between Serdinya and Prades. Their location and their

202   relationship to karstic networks are described in Hez et al. (2015). Alluvial terraces into the

203   Villefranche-de-Conflent gorges are poorly preserved. The T1 terrace (~+20 m) is continuous

204   and well-represented. The T2 terrace (25-30 m) is poorly represented in the gorges and poorly

205   conserved. Within the gorges, the T3 and T4 levels are absent. Altimetric correlations

206   between terraces and cavity levels have been proposed (Calvet et al., 2015, Hez et al., 2015).

207   However, in addition to the fact that the absolute age of the alluvial terraces is poorly

208   constrained, a convincing correspondence remains to be established through notably classical

209   petrological and mineralogical studies and through geochemical characterizations of the

210   source of the material.

211   The study area is drained to a local base level by the Têt and its main tributaries. The

212   Têt is a river that is connected to the Mediterranean domain. This river originates at an

213   altitude of 2405 m in the Carlit massif, pours towards the southeast as it crosses the crystalline

214   massif of Mount-Louis, and then changes direction at Fontpédrouse to flow towards the

215   northeast – southwest along the plane of the Conflent graben (Figure 1). The Cady and the

216   Rotja, which are tributaries along the right bank of the Têt, drain augen orthogneiss and

217   biotite granites, which are represented on most of the Canigou massif. Most of the drainage is

218   confined to canyons with a flat alluvial floor, but a portion of the river or its tributaries seems

219   to be systematically lost over time in the carbonate massifs (Figure 1).

220   **2.2. Karst features and cave systems**

221   The confined karst of Villefranche develops in the Devonian carbonate rocks in the

222   eastern portion of the syncline. This geological unit is characterized by metamorphic

223   limestones and some marbles (Guitard et al., 1998). The syncline extends from west to east

224   over approximately thirty kilometers, with a width of approximately 4 km on its eastern

225   section, where the karstification is most important. The Hercynian major fault of Mérens

226   borders the northern Coronat massif (Figure 1) and confines the karst in the Têt river valley.

227   The Hercynian orogeny would be responsible of the main structuration of the massif.

228   Paleogene compression, which deforms the already folded Paleozoic terrains, has probably

229 reactivated old faults. Thus, a plurikilometric shortening has created significant volumes and
230 allowed the circulation of water in the massifs.
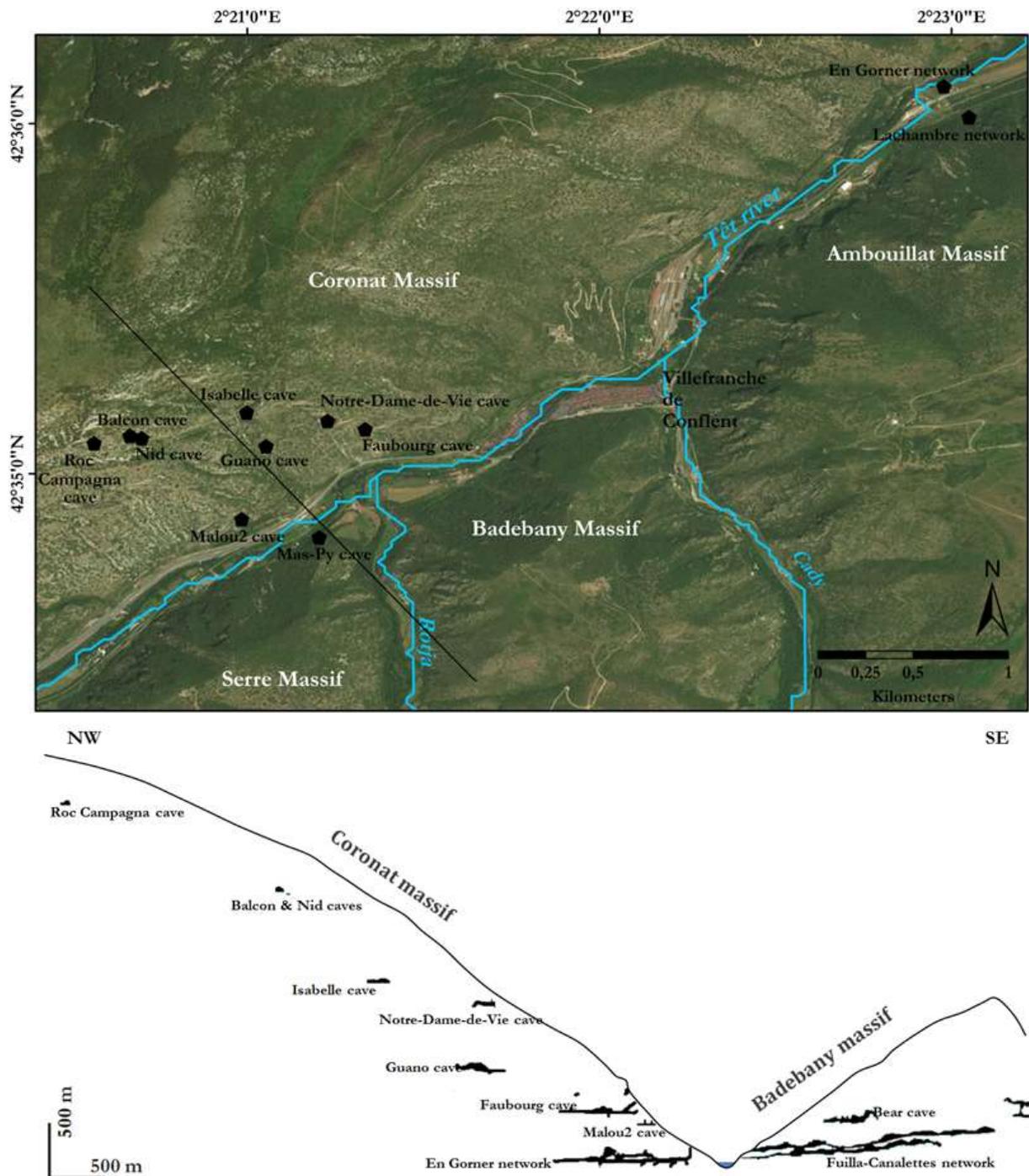
231

232 Figure 2: Map and projected section (modified after Calvet et al., 2015) of the Têt River valley
233   near Villefranche-de-Conflent, which shows the karstic network's spatial distribution and
234   patterns in the massifs. Eight epiphreatic levels are clearly identifiable at the massifs of
235   Badebany (right bank) and Coronat (left bank) and have been investigated. Their
236   establishment is influenced by the Têt and its tributaries, the Cady and the Rotja. The floors
237   close to the current base level are the most developed. The perched levels have probably been
238   trimmed because of the removal of the flanks of the massif over time.

239   Few surface karst features are present in this area, and most of the networks are
240 horizontal. If wells, cascades or potholes were present, they disappeared because of the

backwards slopes or erosion. However, underground karst features are well developed in four main massifs (Coronat in the left bank, Serre, Badebany and Ambouillat in the right bank), which were largely described by Calvet et al. (2015).

We can distinguish eight epiphreatic levels at ~600-m height on a valley transect near Villefranche-de-Conflent (Figure 2; Calvet et al., 2015; Hez et al., 2015). This study area is therefore very original and complex because of the high density of levels in this area, even if this fact is quite classical in the Pyrenees. The first level, which is close to the current base level of the Têt River, corresponds to the large underground networks of the karst of Villefranche. This level is particularly developed, with ~75 km of galleries discovered (En Gorner, Lachambre and Fuilla – Canalettes networks), probably because of a pronounced base-level stationary phase (Audra, 1994). The seven epiphreatic levels above the large karstic systems retain only limited sections of galleries under development because of (i) erosion, which led to the retreat of the southern slope of the massif, thus reducing the size of the horizontal duct; (ii) the total clogging of galleries by gravitational deposits, concretions, and detrital deposits, preventing any speleological exploration towards the logical sequence; and (iii) sudden interruptions of galleries because of faults or fractures, disconnecting the conduits by shifting the blocks of the massif, as observed in the caves of Faubourg and Notre-Dame-de-Vie (Calvet et al., 2015; Hez et al., 2015).

One of the crucial points of this area is the rarely observed inter-connections of sub-horizontal cavities (Hez, 2015; Hez et al., 2015). Indeed, unlike a staggered network, whose levels are inter-connected by vertical wells, the staging of cavities in the Villefranche karst seems to consist of distinct sub-horizontal networks from repeated base-level fluctuations in the Têt River.

Erosion morphologies provide valuable information on previous underground circulations, including the direction of the flows. The waves of erosion that were observed on the walls of the staging cavities support their functioning towards the interior of the massif in the direction of the axis of the Villefranche syncline (Faubourg cave) and parallel to the Têt River (SO-NE), as in the Guano cave and in a majority of the En Gorner network (Hez, 2015; Hez et al., 2015). These stretches of staged epiphreatic levels can therefore correspond to successive self-capture levels of the Têt on the left bank. On the right bank, cavity staging is limited to two or even three levels in the massif, significantly lower than those in the Coronat massif (Figure 2).

3. Methods

3.1. Sampling strategy

3.1.1. Cave sediments

The use of karst as a paleoenvironmental marker and the study of karstic infillings are particularly interesting because karst is a conservative environment in which alluvial sediments are protected from denudation. Sediments are transported to galleries by interrupted streams or stream piracy from an epigeous river, and their analysis enables us to determine their surface origin and their mode of deposition. In addition, karst records the position of the bottom of the valley at some point. Epiphreatic galleries indicate water-table proximity. During valley deepening, various levels of horizontal conduits are generated, with recent networks forming below previously abandoned generations. However, the opposite is also possible during base-level rise (Mocochain et al., 2009; Tassy et al., 2013). Thus, staged karstic systems record the transient positions of previous local base levels, similar to fluvial terraces during valley deepening. The shape of the galleries and the morphologies on the walls describe the modalities of the digging, filling and draining of the galleries (Figure 3a). In any case, the duration of the development of these networks is supposed to be negligible relative to the duration of the processes that are quantified in this work. However, the scale transfer from the average burial duration that is recorded by the analyzed quartz grains to the "age" of the sedimentary deposit that contained them is far from straightforward, as is the subsequent deduction of the "age" of the gallery where the sampling occurred and, *a fortiori*, the "age" of the network. Moreover, the basic assumption that a single burial age can be extrapolated to the entire sedimentary sequence in the same network is not straightforward, which supports collecting several samples along the same unit to have a constant burial age. Furthermore, we must face ill-defined conceptual principles, such as the notion of the formed network. Is a network considered to have been formed when it loses its active karst status and becomes a paleokarst, or is it still in formation when climatic or eustatic processes cause the reuse of its conducts? Moreover, to our knowledge, no studies exist that quantify the required time to form a cavity or a network through pertinent absolute dating, the estimates being essentially based on dissolution and structural criteria. In addition, if these studies exist, such studies would only be relevant in their particular context, with the network formation duration greatly depending on the geological, tectonic, climatic, and eustatic contexts of a given region during the investigated period.

To estimate the incision rate of the main river, the morphology of each gallery was analyzed and the alluvium that was trapped and preserved in these horizontal passages was sampled for absolute dating (Figure 3b, c, d).

The Notre-Dame-de-Vie (+ 275 m; Table 1) and Faubourg (+ 110 m; Table 1) caves have been thoroughly described by Calvet et al. (2015).

Caves	Samples ID	Latitude (°)	Longitude (°)	Elevation (m)	Relative elevation (m)	Development (m)
Puits des Racines	PDR	n.c.	n.c.	443	8	17600
Lachambre	AM	42.600306	2.384164	455	20	26000
Mas-Py	MP	42.580303	2.353403	486	20	100
Malou-2	MA2	42.581167	2.349739	501	43	100
Ours	OU	42.585528	2.367028	515	57	552
Sirach	SI	42.598639	2.405250	487	100	1350
Faubourg	F	42.585447	2.355583	545	110	485
Guano	GU	42.584639	2.350889	600	180	250
Notre-Dame-de-Vie	NDV	42.585846	2.353801	710	275	60
Balcon	BA	42.585139	2.344447	907	500	5
Nid	NID	42.585019	2.345003	914	500	14
Roc Campagna	CAM	42.584778	2.342750	1050	580	30
Roquefumade	RF	42.590344	2.308719	1358	836	120

Table 1: Location of the sampled cavities. The provided altitude is that of the current entrance of the cavities. These levels are horizontal, and the altitude of the paleo-drain varies by only a few meters. The relative altitude is that calculated by projection on a perpendicular plane to the current course of the Têt, ignoring its past shifting. The developments of the cavities are those that are known through current speleological exploration. The coordinates of En Gorner's network entrance cannot be transmitted. The point is placed close on the map of Figure 2, but not at the exact location.

The Lachambre network (+ 20 m; Table 1) is located on the right bank. This network consists of two main galleries that are parallel to the Têt (SW-NE) and intersected by meanders because of SE-NW fractures. Numerous morphologies of fluvial erosion and alluvial deposits (Figure 3c), including large concretions that are marked by scallops, are observed. Notches are visible on the walls of the large ducts, marking the passage of an underground river. The Sirach cave could indicate the paleo-emergence of a higher level to the Lachambre network (Hez, 2015). This atypical cavity largely develops in a Burdigalian limestone tectonic breccia. The Mas Py cave was probably a leakage of the Rotja River that emerged in the Têt valley.

The En Gorner network (+ 8 m; Table 1) is a major cavity in the Coronat Massif that was partially traversed by a river, in which two floors can be discriminated. This network is close to the current level of the Têt. The ducts are mainly oriented SO-NE. These ducts are large (Figure 3a) and exhibit many collapses and highly concretionary areas. Some galleries may still experience water rise during snowmelt periods or prolonged episodes of heavy precipitation. In this case, the downstream siphon of the underground river saturates and returns the unabsorbed quantity to the upper galleries. Leakages of the neighboring Nohèdes valley also could have poured water into and shaped the network (Hez, 2015).
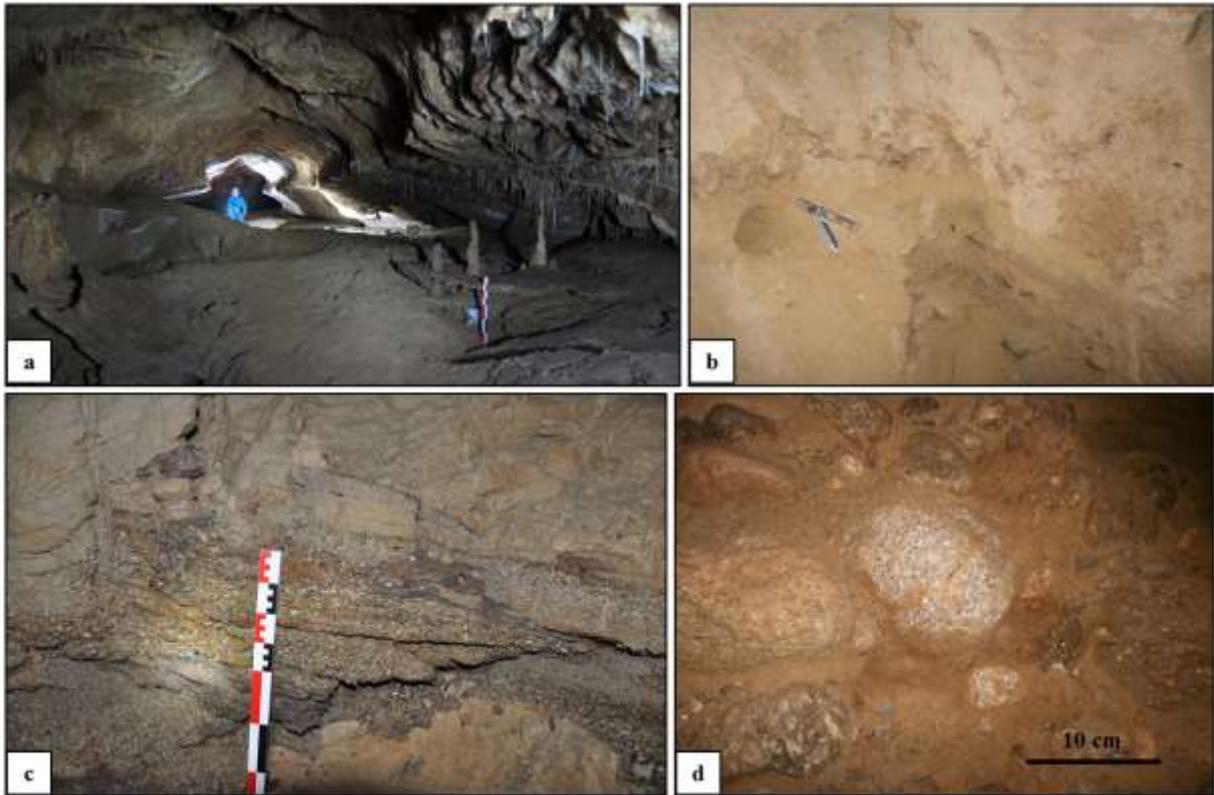
Figure 3: a) Porte de Fer gallery (En Gorner's network), PDR2 sampling site. The morphology of this section is characteristic of the recorded paragenetic regime in the network (Hez, 2015; Hez et al., 2015). The calcite floor, which is visible in the foreground, seals fine deposits. Sand filling partially covers this carbonate deposit. A more recent generation of concretions sporadically seals the deposit. b) PDR7 sampling site in the Sablier (En Gorner's network). The sandy bench is located above the picked pebbles (PDR8 to PDR13). c) AM2 sampling site. Sandy-bedded deposits in the Lachambre network are surmounted by laminated clay loams, indicating a prolonged episode of paragenetism. d) PDR5 to PDR13 sampling sites. Granites and gneiss pebbles in the En Gorner's network. The deposit is massive and clogs the Sablier gallery.

Most of the other prospected cavities (Table 1) that exhibit similar characteristics but were not sampled are small (1 to 2 m wide), except for the main gallery of the Guano cave, which is approximately ten meters wide, similar to the Notre-Dame-de-Vie cave. These differences in cavity size may be related to time-varying paleo-regimes.

The siliciclastic fillings that were trapped in the ducts of the different cavities in the Villefranche karst have variable particle sizes and are found in the form of clay, silt, sand (Figure 3b, c), gravel and pebble (Figure 3d). These detrital fillings were brought by a paleo-Têt and its tributaries (mainly Cady and Rotja) and were conserved in the endokarst at almost all levels of the tier. We sampled amalgams among the few available deposits, provided that we could rely on the classic markers of phreatic and epiphreatic circulation, the geometry of the deposits, and the selected deposit was an alluvial deposit and not an intrakarstic deposit. These deposits consisted of gneiss, granitoid, quartzite, micaceous sands, schist, and micashist at almost all levels of staging. Considering the lithologies in the Têt watershed, the Têt and its tributaries were likely responsible for the transport and deposition of these trapped alluvial

360 deposits in the cavities of the Villefranche karst. The lithologies and particle sizes within each
361 cavity are detailed in Table 4.

362 **3.1.2. Riverbeds**
363

364   To constrain the current denudation rates and concentration ratios, we sampled
365 sediments that were transported by the main active rivers (Figure 4; Table 2), with sand and
366 pebbles being treated separately for comparison.

367   Such sampling was also conducted to analyze the potential effects on the concentration
368 ratios of the collected sediments from alluvial deposits that were remobilized by the rivers
369 before being deposited in the cavities, even if extrapolating the current results to the
370 prospected cavity deposits is inappropriate because of likely different hydrological conditions.
371 Thus, a modern sediment sample was taken upstream of these deposits at Thuès-entre-Valls to
372 detect possible interference from the cosmogenic signal from the Escaro Formation (TT point;
373 Figure 4d).

Location	Samples ID	Latitude (°)	Longitude (°)	Elevation (m)
Têt-Villefranche	TV	42.585722	2.363639	456
Têt-Thuès	TT	42.525000	2.226750	806
Rotja - Fulla	RO	42.578806	2.355861	494
Cady - Canalettes	CAD	42.581694	2.371055	451

374   Table 2: Location and elevation of the four riverbed sediment sampling sites in Figure 4.

375   When possible, we distinguished the lithologies. Certain infrastructures are present
376 upstream of the course of the Têt, especially the Bouillouses dam, which was built between
377 1903 and 1910. Development works have also been conducted along the Rotja River in recent
378 decades. Fortunately, most drains in the watershed do not pass through this point. Moreover,
379 the measurements of cosmogenic nuclide concentrations in modern river samples in different
380 drainage basins enable us to calculate the local catchment-integrated production rates for [26]Al
381 and [10]Be. The use of present-day rivers to determine the past production rate is correct
382 assuming a constant denudation rate and stable altitude for the riverbed.

383   Given their actual drainage networks, the Cady and the Rotja Rivers may have incised
384 the Neogene Escaro Formation (see Supp. Info) and transported embedded sediments, which
385 were included in their bed loads. We must verify such a hypothesis because pebbles that were
386 transported by these tributaries may have been deposited in the studied cavities of the
387 Badebany and Serre massifs. The other massifs in the area, whose drains could potentially
388 feed the Têt, must also be considered. Additionally, we must examine whether this potential
389 influence was attenuated in sands. A much larger number of grains can be analyzed in a sand
390 sample (compared to pebble samples), so sands may more accurately represent the

concentrations of the erosion products of these two sub-watersheds. Therefore, sediments were collected both before the confluence between the Rotja and the Têt, specifically, at the RO point, and after their confluence at the TV point (Figure 4c). The TV point is 1.3 km downstream of the RO point. Finally, we sampled the Cady before its confluence with the Têt (Figure 4b) at the CAD point. At these last three locations, we distinguished the particle sizes and lithologies. We could not collect riverbed sediments after the confluence between the Têt and the Cady because of accessibility issues.

Figure 4: Details of the riverbed sediment sampling sites. The locations are given in Table 2. Pictures were taken during low-water periods. a) Map that shows the four sampling locations (white dots) and their relationships with both the Miocene Escaro Formation (in yellow) and cave entrances (red dots). b) Cady sampling site. The riverbed is 5-7 m wide and contains metric blocks. The flow is torrential, and particle sizes smaller than coarse sands were absent, even on the banks. c) Villefranche-de-Conflent sampling site on the Têt river. The particle sizes range from fine sands on the banks to metric blocks within the bed of the river. d) Thuès-entre-Valls sampling site. The riverbed's width does not exceed five meters, and the flow is torrential. At this point, the river flows on steeper slopes. Particle sizes smaller than coarse sands were absent, even on the banks.

3.1.3. Escaro Formation

The Escaro Formation was sampled to determine whether the cosmogenic nuclide ratios of the material that enters the caves are significantly affected by the potential complex

burial/re-exposure histories of its components (Table 3). While some authors assigned a Miocene age to the Escaro Formation (Guitard et al. (1998) and references therein), other authors assumed this formation as being a component of a late Pliocene set (e.g., Clauzon et al., 2015 and references therein). Solving this controversy is beyond the scope of this study. The samples were collected from a quarry that was exploited at the beginning of the last century for hematite and fluorite. According to the aforementioned authors, it should be pointed out that this quarry may equally well be found in the Escaro Formation as in a gneissic thrust slice of the olistoliths. In the end, it does not matter, some of these slices being intercalated in the Escaro Formation (e.g., Oele et al., 1963). In the western area of the basin between Prades and Escaro, the yellowish formation consists of an alternation of very poorly sorted quartz-feldspathic sands and essentially gneissic metric-sized block levels (Guitard et al., 1998). The predominance of gneiss indicates that the Canigou massif is the main source of the clasts, which is reasonable because of the large exhumation of the massif in response to the opening of the Gulf of Lion (Maurel et al., 2008). The base of the formation has a large dip of approximately 30° towards the N-NE at the outcrop (Figure 5). This formation's thickness, which is at least 600 m, can be estimated north of Escaro. The degrees of alteration vary. It is worth noting that there is apparently no paleosoils within the Escaro formation.

Gneiss pebbles, quartzite pebbles and sands were separately analyzed in the samples EB1, EB2 and EB3 from the base of the formation to distinguish particle sizes and lithologies. The same protocol was applied to one of the samples (ET1, ET2 and ET3) from the mid-slope bench, which enabled us to quantify the accumulation rates.

Location	Samples ID	Latitude (°)	Longitude (°)	Elevation (m)
Escaro quarry - halfway up bench	ET	42.543278	2.313500	926
Escaro quarry - base of the formation	EB	42.542972	2.308694	951

Table 3: Location and elevation of the two Escaro quarry sampling sites in Figure 5.
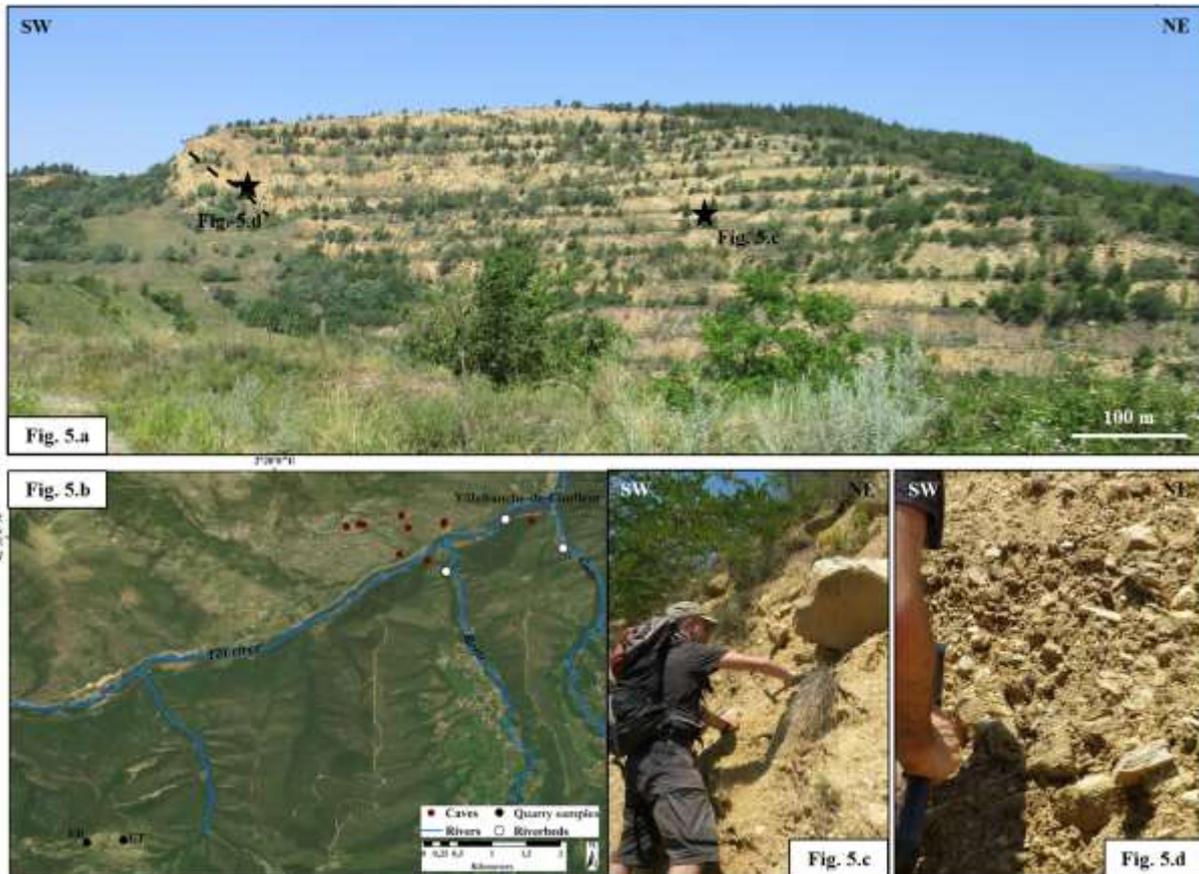
Figure 5 : Escaro quarry site. The locations are given in Table 3. a) Panorama of the quarry that was exploited during the 20th century. The re-exposure period is negligible, and the selected sites are properly shed under more than 30 m of sediment. The base of the supposed Miocene formation is plotted with a dip of 30° to the NNE. b) Map that shows the two sampling locations (black dots) and their relationships with both the three riverbed sampling sites (white dots) and cave entrances (red dots). EB represents the base of the formation samples and ET the halfway-up crossing samples. c) Halfway-up bench-sampling site. The particle sizes range from medium sands to gneiss metric blocks. d) Base of the formation sampling site, which is mainly sandy deposits and clasts of gneiss and quartzites.

3.2. Burial duration determination systematics

The burial dating method is based on the differential radioactive decay of two cosmogenic nuclides, which accumulate in quartz minerals of surface rocks that are exposed to cosmic rays. At a depth of 8–10 m, in situ-production from neutrons is stopped, and muons represent only 1% of the total surface production, so the significant burial of the sample of interest halts the in situ production of cosmogenic nuclides. The concentrations of initially accumulated radionuclides (^{26}Al and ^{10}Be) then decrease as a function of their respective half-lives. Knowing the production ratio of the cosmogenic nuclides of interest in quartz minerals, enables us to determine their burial age and the maximum denudation rates that prevailed in the source area before the samples were buried by measuring the ^{26}Al/^{10}Be and/or ^{10}Be/^{21}Ne ratios in the samples.

Caves provide a nearly ideal configuration for such burial duration determinations because exposure to cosmic rays since the burial episode is usually negligible. The galleries

458   of the caves that were sampled in this study are always overlain by more than 30 m of rocky

459   material in all directions, therefore making post-burial production negligible. The accuracy of

460   the results (^{26}Al/^{10}Be = R$_{AB}$) relies on the following assumptions: (i) the quartz from which

461   the TCN are extracted was exposed long enough at the surface to accumulate measurable

462   concentrations of cosmogenic radionuclides; (ii) the transport time before burial was

463   negligible compared to the exposure duration to cosmic rays on a surface under a denudation

464   regime, so the storage duration within the catchment was limited; and (iii) burial was rapid

465   and deep enough to avoid cosmogenic nuclide post-burial production.

466   **3.2.1. ^{26}Al/^{10}Be based burial duration determination**

467

468   A rock that is exposed to cosmic radiation accumulates terrestrial cosmogenic nuclides

469   (TCN) such as ^{26}Al and ^{10}Be, whose concentrations can be calculated by using the following

470   equation (Braucher et al., 2011):

471      $C(x, \varepsilon, t) =$

472
$$C(x, \varepsilon', t') \exp(-\lambda t) + \frac{P_{sp}.\exp\left(-\frac{x}{L_n}\right)\left(1-\exp\left(-t\left(\frac{\varepsilon}{L_n}+\lambda\right)\right)\right)}{\frac{\varepsilon}{L_n}+\lambda} +$$

473
$$\frac{P_{\mu slow}.\exp\left(-\frac{x}{L_{\mu slow}}\right)\left(1-\exp\left(-t\left(\frac{\varepsilon}{L_{\mu slow}}+\lambda\right)\right)\right)}{\frac{\varepsilon}{L_{\mu slow}}+\lambda} + \frac{P_{\mu fast}.\exp\left(-\frac{x}{L_{\mu fast}}\right)\left(1-\exp\left(-t\left(\frac{\varepsilon}{L_{\mu fast}}+\lambda\right)\right)\right)}{\frac{\varepsilon}{L_{\mu fast}}+\lambda}$$

474   (eq. 1)

475   where C(x,ε,t) is the nuclide concentration as a function of the attenuation depth *x*

476   (typically expressed as a function of depth *z*, in cm, and bedrock density *ρ*, in g/cm^3),

477   denudation rate *ε, ε*' (in g/cm^2/a), and exposure times and t'*t* (in years). The term $C(x, \varepsilon', t')$

478   is the inherited concentration. P$_{sp}$, P$_{\mu slow}$, and P$_{\mu fast}$ and L$_{sp}$ (160 g/cm^2), L$_{\mu slow}$ (1500 g/cm^2),

479   and L$_{\mu fast}$ (4320 g/cm^2) (Braucher et al., 2011) are the production rates and attenuation lengths

480   of neutrons, slow muons and fast muons, respectively; *λ* is the radioactive decay constant of

481   the TCN under investigation. C(x,0) is the ^{10}Be or ^{26}Al concentration that is acquired during

482   periods of exposure time prior to denudation.

483   The chemical procedure for ^{10}Be and ^{26}Al extraction from all the samples to measure

484   their ^{10}Be and ^{26}Al concentrations was conducted at CEREGE (Aix-en-Provence, France) and

485   followed Brown et al. (1991) and Merchel and Herpers (1999). Pebbles were crushed and

486   sieved (250-800-µm fraction). Quartz was concentrated through magnetic separation and

487   selective dissolution in a 1/3 HCl – 2/3 H$_2$SiF$_6$ mixture. Quartz was decontaminated from the

488   atmospheric ^{10}Be by dissolving 30% in mass through three successive HF leaching steps. Pure

quartz was then spiked with 100 µL of a (3025 ± 9)-ppm in-house ^{9}Be carrier (Merchel et al., 2008) and with an adapted amount of a 985 µg/g ^{27}Al carrier. The natural ^{27}Al concentrations in the dissolved samples were measured by inductively coupled plasma optical emission spectrometry (ICP-OES) on an ICAP6500 Thermo Scientific unit spectrometer. We performed this analysis of replicate aliquots using two emission lines (394 and 396 nm, axial sight) and two standards (Merck of 999 ± 2 mg/L, and Fluka TraceCert of 985 ± 2 µg/g). Finally, dissolution was conducted in concentrated HF.

The abundance of muscovites (with high ^{27}Al content) in the rocks from the watershed forced us to regularly check the purification of the samples with a binocular microscope. If not removed from the quartz before total dissolution, these muscovites would cause the formation of thick solid crusts, from which properly recovering all the dissolved aluminum would become difficult.

BeO and Al_2O_3 were then purified and extracted by using a succession of alkaline precipitation and separations on ionic-exchange resins (used exchange resins: DOWEX 1x8 100–200 mesh, DOWEX 50Wx8 100–200 mesh). Finally, full oxidization was performed at 700°C for one hour. The obtained BeO and Al_2O_3 oxides were mixed with Nb and Ag conductive powders, respectively, and then introduced in a copper cathode to be pressed. The ^{10}Be/^{9}Be and ^{26}Al/^{27}Al ratios were finally measured at the French national AMS facility ASTER. The measured ^{10}Be/^{9}Be ratios were calibrated against the ^{10}Be/^{9}Be SRM 4325 NIST (National Institute of Standards and Technology) standard with an assigned value of $(2.79 \pm 0.03)\cdot10^{-11}$ (Nishiizumi et al., 2007). The measured ^{26}Al/^{27}Al ratios were calibrated against the ASTER in-house standard SM-Al-11, whose nominal value is ^{26}Al/^{27}Al $= (7.401 \pm 0.064)\cdot10^{-12}$ (Merchel and Bremser, 2004). The half-lives (^{10}Be: 1.387 ± 0.012 Ma (Korschinek et al., 2010; Chmeleff et al., 2010); ^{26}Al: 0.717 ± 0.024 Ma (Samworth et al., 1972)) and the standardization method that were used at ASTER (SM-Al-11/07KNSTD) implied that the ^{26}Al/^{10}Be spallation production ratio was ~6.61 ± 0.52. Analytical uncertainties included the counting statistics, the machine's stability (~0.5%; Arnold et al., 2010 for ^{10}Be) and blank correction.

All the calculations were conducted with a sea-level, high-latitude (SLHL) ^{10}Be spallation production rate of 4.01 ± 0.18 at g^{-1} a^{-1} (Borchers et al., 2016), which was assumed to be constant over time and scaled for latitude (Stone, 2000) and elevation. Corrections for mass shielding were calculated by using the equation of Dunai (2009). Muon contributions from Braucher et al. (2011) were only scaled for altitude. The production rate is calculated for each cell of the 30 m ASTER DEM and the 9.03 ± 0.95 at/g(Qz)/yr mean catchment production rate is computed following a Matlab script and the CREp tool (Martin et al., 2017), using a

524 rock density of 2.5 g/cm^3. Areas without quartz-bearing rocks and not linked to the stream
525 network were excluded from calculations. No corrections were performed for ice cover since
526 it only represents a very small proportion of our studied area. We used the globally averaged
527 P10 obtained in CREp and the 21/10 production ratio (P21/P10=4.13) defined in Kober et al.
528 (2007).

529 ### 3.2.2. ^{10}Be/^{21}Ne-based burial duration determination
530

531 The cosmogenic burial dating method was based on the evolution of the ^{26}Al/^{10}Be
532 ratio and limited to the last ~6 Ma, so we had to expand the investigated period to pinpoint the
533 chronology of the valley incision. Thus, we implemented the cosmogenic burial dating
534 method based on the evolution of the ^{10}Be/^{21}Ne ratio.

535 The neon isotopes, whose concentrations were measured on the Helix-SFT™ mass
536 spectrometer at CRPG (Nancy, France), originated from both the fluid inclusions in the quartz
537 minerals and the surface of the quartz grains. The same quartz fractions (250 – 800 μm) as
538 those that were used to determine the ^{26}Al and ^{10}Be concentrations were analyzed (same
539 sample splits), even if the finest fraction was more suitable to reduce the contribution of
540 atmosphere-like Ne that was trapped in the fluid inclusions. All the samples were wrapped in
541 tin foil and loaded into the carousel of a new induction furnace that was designed at the
542 CRPG lab (Zimmermann et al., 2017). Following conclusive validation tests, neon was
543 extracted in one single heating step at ~1500°C over at least 25 min. Atmospheric
544 contamination was low enough to ensure a proper estimate of the non-cosmogenic
545 component. After gas extraction by heating, chemically active gases were removed in two Ti
546 sponge getters; Ar–Kr–Xe was trapped in a charcoal finger at liquid-nitrogen temperature. Ne
547 was cryo-focused at 35 K before being released at 90 K. The neon concentrations and isotopic
548 compositions were determined via peak jumping mass spectrometry by using detectors with
549 multipliers. Neon isotopes were corrected for isobaric interferences, instrumental mass
550 fractionation and analytical blanks. Aliquots of the quartz standard CRONUS-A that were
551 measured during the sample batch yielded a ^{21}Ne excess of (331 ± 6).10^6 at/g, which matched
552 the reference concentration of (348 ±10).10^6 at/g (Vermeesch et al., 2015).

553 The cosmogenic component was computed by using the following formula:

$$^{21}\text{Ne}_{\text{cosmogenic}} = {}^{21}\text{Ne}_{\text{sample}} - {}^{20}\text{Ne}_{\text{atmospheric}} \times \left(\frac{^{21}\text{Ne}}{^{20}\text{Ne}}\right)_{\text{air}}$$

554   The concentration of excess ^{21}Ne ($^{21}Ne*$) was determined as follows (Vermeesch et
555   al., 2015):

$$^{21}Ne^* = R_c \times {}^{20}Ne_m \times \frac{R_m - R_a}{R_c - R_a}$$

556   where $^{20}Ne_m$ is the measured neon-20 concentration; $R_c = 1.1$, the cosmogenic
557    $^{21}Ne/^{20}Ne$ production ratio (Niedermann, 2002); R_m is the measured $^{21}Ne/^{20}Ne$ ratio; and $R_a =$
558   0.002905, the atmospheric $^{21}Ne/^{20}Ne$ ratio (Honda et al., 2015).

559
560   **4. Results**
561
562   **4.1. ^{10}Be and ^{26}Al**
563
564   All the measured ^{10}Be and ^{26}Al concentrations and the resulting $^{26}Al/^{10}Be$ ratios with
565   their associated uncertainties are presented in Table 4. $^{10}Be/^9Be$ ratios that were significantly
566   different from the background value, the mean analytical blank $^{10}Be/^9Be$ ratio being $(2.94 \pm$
567    $0.21).10^{-15}$, were measured for all samples but F4C. They lead to ^{10}Be concentrations ranging
568   from (0.40 ± 0.06) to $(51.1 \pm 17.5).10^4$ atoms per gram. .

569   Some of the measured $^{26}Al/^{27}Al$ ratios were not significantly different from the
570   analytical blank $((1.31 \pm 0.56).10^{-15})$, which suggests burial durations outside the
571   methodological framework. For the remaining samples, the ^{26}Al concentrations range between
572   (1.25 ± 0.74) and $(84.32 \pm 5.51).10^4$ atoms per gram.

573   Only the $^{10}Be/^9Be$ ratios were measured in the samples from the Ours, Guano, Balcon,
574   Nid, Roc Campagna, Roquefumade and Notre-Dame-de-Vie caves because of their high
575   muscovite content (for the first two cases) or because of their $^{26}Al/^{27}Al$ ratios not significantly
576   different from the background value.

577   All the burial durations and the derived maximum paleo-denudation rates (denudation
578   rates that prevailed before the burial event (ε' in equation 1), which were calculated by using
579   either the $^{26}Al/^{10}Be$ ratios or the $^{10}Be/^{21}Ne$ ratios, are presented in Table 6. In the river sands,
580   the measured ^{10}Be and ^{26}Al concentrations were assumed to indicate the concentration of all
581   quartz-bearing rocks that outcropped in the drainage basin, in addition to a sufficiently long
582   exposure duration to reach a ^{10}Be - ^{26}Al steady-state concentration (Brown et al., 1985). Thus,
583   we could determine the average denudation rate for an entire drainage basin by measuring the
584   cosmogenic nuclide concentration in riverbed sands. Tests with coherent sensible variations
585   did not lead to significant differences, so an average paleo-elevation of the catchment basin
586   that was similar to the current value was assumed.

	Sample	Site	Facies and lithologies	^{10}Be (kat/g)	^{26}Al (kat/g)	^{26}Al/^{10}Be
Caves	PDR1	Puits des Racines	6 amalgamated pebbles (quarzites, gneiss, granites)	39.13±5.66	55.96±20.26	1.43±0.56
	PDR2	Puits des Racines	Sand, fine	113.76±9.09	79.96±10.91	0.70±0.11
	PDR3	Puits des Racines	Sand, medium to coarse	116.29±4.27	569.17±42.07	4.89±0.40
	PDR4	Puits des Racines	15 amalgamated pebbles & gravels (quarzites, gneiss, granites)	126.11±11.15	159.42±25.78	1.26±0.23
	PDR6	Puits des Racines	4 amalgamated weathered granites pebbles	8.42±0.97	20.99±8.06	2.49±1.00
	PDR7	Puits des Racines	Sand, medium	71.99±4.48	477.82±47.18	6.64±0.77
	PDR8	Puits des Racines	Quartzite pebble	29.86±3.65	125.42±27.33	4.20±1.05
	PDR10	Puits des Racines	Gneiss pebble	4.05±0.60	17.24±12.75	4.26±3.21
	PDR12	Puits des Racines	Quartzite pebble	102.87±6.23	542.57±55.72	5.27±0.63
	PDR13	Puits des Racines	Granite pebble	15.03±4.38	23.78±17.38	1.58±1.25
	AM1	Lachambre	Clast-supported gravel	101.11±5.03	B.D.L	-
	AM2	Lachambre	Sand, medium to coarse	120.27±10.31	133.33±41.48	1.11±0.36
	AM3	Lachambre	7 amalgamated pebbles (quarzites, gneiss, granites)	67.00±7.63	B.D.L	-
	AM4	Lachambre	8 amalgamated pebbles (quarzites, gneiss, granites)	203.78±11.97	555.72±70.56	2.73±0.38
	AM5	Lachambre	4 amalgamated pebbles (quarzites, gneiss, granites)	99.60±6.78	388.99±85.26	3.91±0.90
	AM6	Lachambre	3 amalgamated pebbles (quarzites, gneiss, granites)	101.40±5.21	155.86±24.20	1.54±0.25
	AM7	Lachambre	8 amalgamated gneiss pebbles	116.29±5.39	640.06±65.94	5.50±0.62
	AM8	Lachambre	10 amalgamated granites pebbles	72.01±8.35	81.61±27.37	1.13±0.40
	AM9	Lachambre	8 amalgamated granites pebbles	511.22±17.71	2932.44±236.36	5.74±0.50
	MP1	Mas-Py	Amalgamated pebbles and sands (fine to coarse)	134.54±6.25	B.D.L	-
	MP2	Mas-Py	Medium to very coarse sand, may be pebbly	171.11±7.12	398.42±74.13	2.33±0.44
	MP3	Mas-Py	Sand, medium to coarse	150.17±11.07	91.35±9.96	0.61±0.08
	MA2-1	Malou-2	Sand, medium	127.25±5.74	256.72±58.91	2.02±0.47
	OU1	Ours	Clast-supported gravel	84.23±10.83	B.D.L	-
	OU2	Ours	Clast-supported gravel	68.78±11.34	B.D.L	-
	GU1	Guano	Coarse to very coarse sand, may be pebbly	85.06±4.83	B.D.L	-
	GU2	Guano	Sand, fine to locally loamy	56.78±2.66	B.D.L	-

	Sample	Location	Description			
	Si1	Sirach	Matrix supported very coarse to pebbly sandstones	119.03±8.84	57.67±19.31	0.48±0.17
	F1S	Faubourg	Sand, fine to medium	68.68±10.30	71.40±21.61	1.04±0.35
	F2S	Faubourg	Sand, fine to medium	171.65±45.62	39.53±20.09	0.23±0.13
	F3S	Faubourg	Sand, medium to coarse	132.02±7.92	37.18±13.25	0.28±0.10
	F2A	Faubourg	3 amalgamated unweathered granites pebbles	125.92±19.55	108.38±38.35	0.86±0.33
	F2B	Faubourg	2 amalgamated growan pebbles	105.04±10.46	71.16±15.5	0.68±0.16
	F2C	Faubourg	3 amalgamated unweathered gneiss pebbles	38.78±5.80	63.56±13.89	1.64±0.43
	F2D	Faubourg	2 amalgamated weathered gneiss pebbles	40.77±4.84	15.43±7.79	0.38±0.20
	F3	Faubourg	Granite pebble	89.33±6.18	19.86±4.06	0.22±0.05
	F4A	Faubourg	Gneiss pebble	41.25±7.63	B.D.L	-
	F4B	Faubourg	Quartzite pebble	29.73±4.40	41.92±17.66	1.41±0.63
	F4C	Faubourg	3 amalgamated unweathered granites pebbles	B.D.L	42.72±24.67	-
	NDVG	Notre-Dame-de-Vie	Amalgamated pebbles (quarzites, gneiss, granites)	34.51±2.26	B.D.L	-
	BA2	Balcon	5 amalgamated quartzite pebbles	20.75±4.16	B.D.L	-
	BA3	Balcon	Sand, medium	16.72±2.43	B.D.L	-
	NID1	Nid	Fine to medium rubbish sand	10.29±1.68	B.D.L	-
	NID2	Nid	Sand, Fine to medium	11.10±2.55	B.D.L	-
	CAM1	Roc Campagna	Matrix supported medium to coarse pink sandstones	7.02±1.38	B.D.L	-
	RF3	Roquefumade	Fine to very coarse rubbish sand, may be pebbly	87.59±5.75	B.D.L	-
Riverbeds	CAD1	Cady - Canalettes	8 amalgamated granite pebbles	149.91±19.43	213.33±24.27	1.42±0.25
	CAD1b	Cady - Canalettes	10 amalgamated quartzite pebbles	105.41±5.27	502.04±49.92	4.76±0.53
	CAD2	Cady - Canalettes	Sand, coarse	133.92±10.46	756.97±112.30	5.65±0.95
	RO1	Rotja - Fulla	9 amalgamated granite pebbles	51.10±4.72	102.90±19.64	2.01±0.43
	RO1b	Rotja - Fulla	10 amalgamated quartzite pebbles	80.62±6.36	225.63±31.38	2.80±0.45
	RO2	Rotja - Fulla	Sand, coarse	119.90±11.66	346.43±60.39	2.89±0.58
	TT1	Têt-Thuès	Sand, coarse to very coarse	152.90±8.55	843.20±55.14	5.51±0.47
	TT2	Têt-Thuès	11 amalgamated quartzite pebbles	96.12±9.07	499.60±39.51	5.20±0.64
	TT3	Têt-Thuès	10 amalgamated granite pebbles	28.66±3.47	172.01±25.59	6.00±1.15
	TV1	Têt-Villefranche	Sand, medium to coarse	117.0±9.03	581.41±38.28	4.97±0.5

	TV2	Têt-Villefranche	12 amalgamated quartzite pebbles	93.88±7.20	226.45±30.07	2.41±0.37
	TV3	Têt-Villefranche	12 amalgamated granite pebbles	73.95±10.80	59.05±14.42	0.80±0.23
Escaro formation	EB1	Escaro quarry - base of the formation	5 amalgamated quartzite pebbles	9.58±1.13	27.88±12.48	2.91±1.35
	EB2	Escaro quarry - base of the formation	6 amalgamated altered gneiss pebbles	10.86±2.45	20.02±20.01	1.84±1.89
	EB3	Escaro quarry - base of the formation	Sand, fine to medium	9.62±1.19	12.55±7.37	1.30±0.78
	ET1	Escaro quarry - halfway up bench	7 amalgamated altered gneiss pebbles	6.55±1.24	57.88±33.86	8.84±5.43
	ET2	Escaro quarry - halfway up bench	6 amalgamated quartzite pebbles	24.59±5.10	31.11±8.63	1.26±0.44
	ET3	Escaro quarry - halfway up bench	Sand, fine to medium	8.90±0.97	18.26±6.00	2.05±0.71

Table 4: ^{10}Be and ^{26}Al concentrations at all the sampling sites in their corresponding caves. B.D.L means "below detection limit".

A significant dispersion of the cosmogenic nuclide ratios independent of the stage within the same cave, which led to significantly different burial durations, was highlighted (Tables 4 and 5) for the Lachambre network (AM samples), the En Gorner network (PDR samples) and the Mas-Py cave (MP samples). The Faubourg cave contained two distinct populations: one was centered on a ^{26}Al/^{10}Be ratio of (0.89 ± 0.17), which implies a burial duration of roughly 3 Ma, and another was centered on a ^{26}Al/^{10}Be ratio of (0.27 ± 0.08), which implies a burial duration of roughly 6 Ma. Determining whether the samples with a deduced burial duration of ~3 Ma are an exception or if the cavity would have undergone two episodes of filling is difficult because the geometry of the deposits does not provide any clues to this subject. Concerning these samples, no influence from the analyzed lithology or the size of the particles could be considered (Table 4).

At the most upstream point at Thuès-entre-Valls (TT1, TT2 and TT3 samples; Table 4), the ^{26}Al/^{10}Be ratios are inter-consistent no matter the particle size or lithology. The same trend was observed for the Rotja samples (RO1, RO1b and RO2; Table 4). Their ^{26}Al/^{10}Be ratios indicated burial episodes, so the Rotja samples could have been buried in the Rotja catchment before being remobilized by the river. The ^{26}Al/^{10}Be ratios of the Cady (CAD1, CAD1b and CAD2; Table 4) were scattered, and the pebbles indicated burial episodes. Moreover, the ^{26}Al/^{10}Be ratios of quartzites were similar to those of sands but were significantly different from those of granites. Finally, the ^{26}Al/^{10}Be ratios of the samples from the Têt at Villefranche-de-Conflent (TV1, TV2 and TV3; Table 4) after the confluence with the Rotja were scattered and significantly different from those of the Thuès-entre-Valls (TT1, TT2 and TT3) samples. This difference was particularly striking for the granite pebbles.

**4.2. ^{21}Ne**

All the neon measurements are presented in Table 5.

All the samples in the neon three-isotope diagram (Figure 6) plotted on the spallation line because of their associated uncertainties, which confirms the cosmogenic origin of the ^{21}Ne and ^{22}Ne in excess relative to the atmospheric end-member. In addition, the re-extractions that were conducted between 1446 and 1469°C were not significantly different from the background, demonstrating that all the neon had been initially extracted.

No ^{21}Ne concentrations were determined for the samples from caves at the base of the staging (AM4 (Lachambre network), OU1 (Ours cave) and PDR3 (En Gorner network)) because the measured ratios were not significantly different from those in the air.

Sample	Cave	Mass (mg)	$^{21}Ne^*/^{20}Ne^*$ (x10³)	$^{22}Ne^*/^{20}Ne^*$ (x10)	^{20}Ne (Gat/g)	^{21}Ne (Mat/g)
MP2	Mas-Py	111.8	2.905±0.041	1.009±0.007	4.62±0.31	0.59±0.19
MA2-1	Malou-2	109.0	3.227±0.052	1.008±0.008	3.76±0.25	1.77±0.2
Si1	Sirach	165.3	3.496±0.052	1.005±0.007	2.78±0.18	2.1±0.14
F1S	Faubourg	289.9	3.604±0.2	1.045±0.033	1.29±0.05	1.02±0.26
F2S	Faubourg	382.4	3.472±0.051	1.044±0.008	1.7±0.06	1.12±0.09
F3S	Faubourg	300.6	3.176±0.044	1.042±0.007	2.91±0.1	1.03±0.13
GU1	Guano	111.0	3.637±0.081	0.998±0.013	2.16±0.14	1.96±0.18
NDVG	Notre-Dame-de-Vie	363.3	3.338±0.061	1.048±0.009	2.4±0.08	1.24±0.15
BA2	Balcon	336.1	3.576±0.045	1.072±0.008	3.17±0.11	2.42±0.14
BA3	Balcon	300.4	3.423±0.03	1.051±0.007	2.86±0.1	1.74±0.09
NID2	Nid	284.2	3.845±0.073	1.049±0.012	1.57±0.05	1.63±0.11
CAM1	Roc Campagna	264.8	3.877±0.035	1.031±0.004	6.78±0.45	7.88±0.24
		225.7	3.9±0.049	1.01±0.006	6.59±0.44	7.91±0.32
AM4	Lachambre	126.1	2.649±0.043	1.001±0.007	4.11±0.27	-
OU1	Ours	82.8	2.799±0.095	0.989±0.016	2.35±0.16	-

622   Table 5: Ne isotope ratios and derived cosmogenic ^{21}Ne concentrations.

623   The Balcon and Nid caves, which are located at the same elevation, produced similar

624   ^{10}Be/^{21}Ne burial durations: their ^{26}Al/^{27}Al ratios were not significantly different from the

625   background value because of the complete radioactive decay of all their initially accumulated

626   ^{26}Al.
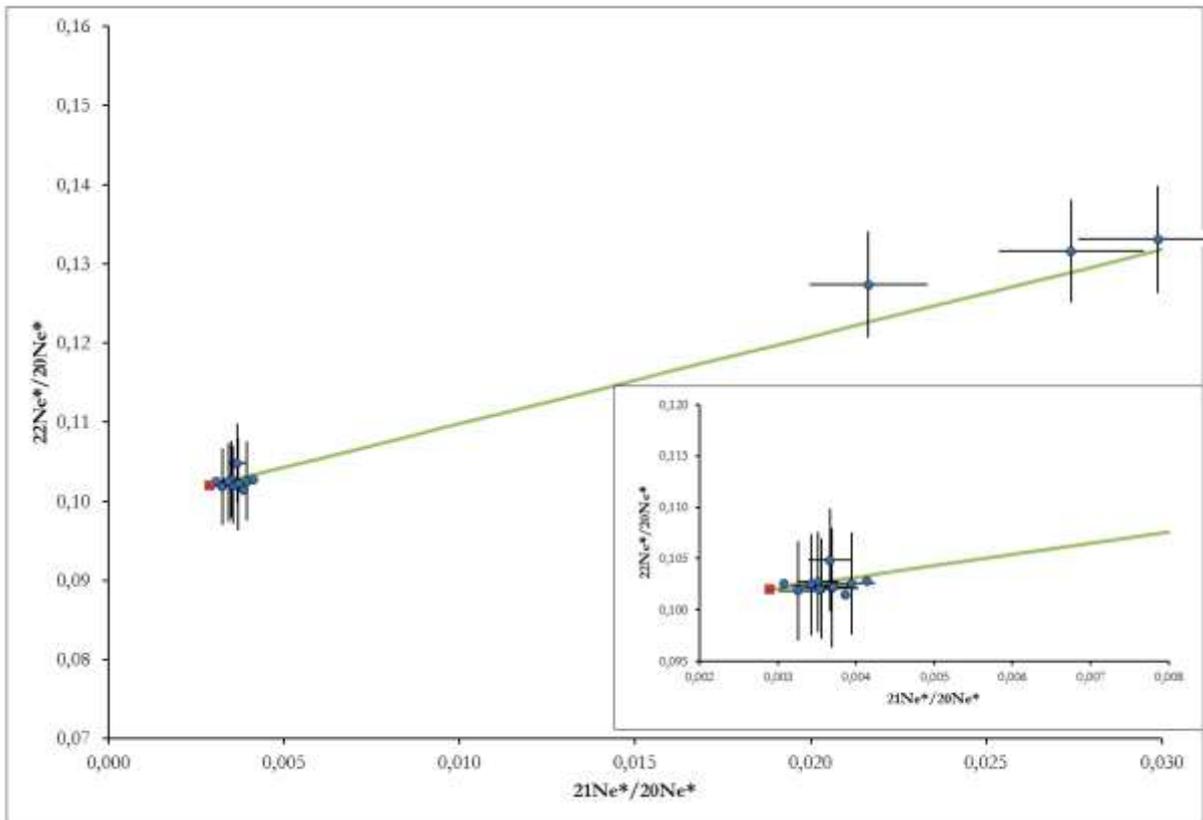
628   Figure 6: Neon three-isotope diagram of the quartz samples from the Têt river catchment. Most of the
629   data from the Têt samples (blue circles) plot on the green spallation line.

630

5. Discussion

5.1. Methodological implications

5.1.1. Usefulness of ^{26}Al/^{10}Be and ^{10}Be/^{21}Ne comparisons

Although the ^{26}Al-^{10}Be-^{21}Ne combination is the most obvious to solve the inconsistencies and enhance the validity of the proposed burial durations, a thorough comparison of the burial durations from samples within the same deposits with both implemented burial dating methods is difficult within the framework of this study. Indeed, the most perched stages had measured ^{26}Al/^{27}Al ratios that were not significantly different from the background, and the cosmogenic neon concentrations within the samples from the Lachambre and En Gorner networks were below the detection limit.

Nevertheless, when possible, this comparison is informative. For the highest caves in which this comparison is possible (Faubourg (F2S and F3S) and Sirach (Si1)) and in the Mas-Py (MP2) cave, the burial durations that were deduced by using both burial dating methods agreed within the uncertainties (Table 6; Figure 7). An interesting case concerned the samples from the lowest floors of the Malou2 cave (MA2-1) and Faubourg cave (F1S). The ^{26}Al/^{10}Be ratios of these samples were reassessed (Calvet et al., 2015), and the burial durations from their respective ^{26}Al/^{10}Be and ^{10}Be/^{21}Ne ratios were significantly different. We propose that these differences may reflect either complex histories of multiple burials and re-exposures or mixtures of sediments of different ratios. Although the ^{26}Al/^{10}Be ratio could recover its surface value through multiple burials and re-exposures, this phenomenon is most likely not possible for the ^{10}Be/^{21}Ne ratio because ^{21}Ne is a stable isotope. This finding is coherent with the ^{26}Al/^{10}Be-deduced burial duration, which was roughly 2 times lower than the ^{10}Be/^{21}Ne-deduced burial duration. Regarding the second proposition, mixtures of sediments of different ratios may occur between two levels that are linked by a vertical connection or may result from external events, such as (i) more pronounced basal stagnation phases (as it is potentiality the case in Arkansas (Keen-Zebert et al., 2016; Paces et al., 2017)) with the remobilization of previous deposits; or (ii) substantial fluctuations in the base level, which led to the partial re-use of the ducts, remobilization of previous deposits, and potential refreshment of the morphologies. Indeed, if the sediments have not had time to consolidate, their remobilization may have erased old morphologies. However, this last hypothesis seems likely because of the on-site remodeling of sand or pebbles from 4 to 7 Ma. Indeed, these networks seem to have fluvial sediments that form the same sedimentary deposit. This hypothesis is difficult to verify with few stratigraphic elements that could also be linked to the ultimate deposition phase in some cavities. Nevertheless, this hypothesis might explain why "free" sands (PDR2, for example) have higher burial durations than consolidated sands in stratigraphy or clasts.

5.1.2. Cave dating and inheritance: riverbeds and Escaro Formation

In the context of the second hypothesis, we investigated one of the most significant sedimentary deposits in the study area, namely, the Escaro Formation, to examine the potential influence of sediments that are drained at the surface from sedimentary deposits on the measured cosmogenic nuclide ratios in cave deposits. The formation of the Col de Fins, which is supposedly of Neogene age, and the terrace levels were not considered here but could have also played a role.

Sample	Site	$^{26}Al/^{10}Be$ burial duration (Ma)	$^{10}Be/^{21}Ne$ burial duration (Ma)	Derived paleodenudation rate (cm/ka)
PDR1	En Gorner	3.12±0.8		11.4±1.7
PDR2	En Gorner	4.58±0.33		3.9±0.3
PDR3	En Gorner	0.58±0.17		3.8±0.1
PDR4	En Gorner	3.37±0.38		3.5±0.3
PDR6	En Gorner	1.97±0.83		53.3±6.1
PDR7	En Gorner	0.12±0.24		6.2±0.4
PDR8	En Gorner	0.9±0.51		15±1.8
PDR10	En Gorner	0.87±1.55		110.8±16.4
PDR12	En Gorner	0.43±0.25		4.3±0.3
PDR13	En Gorner	2.91±1.62		29.8±8.7
AM2	Lachambre	3.65±0.89		5.1±0.4
AM4	Lachambre	1.82±0.41		3±0.2
AM5	Lachambre	1.05±0.47		4.5±0.3
AM6	Lachambre	2.97±0.34		4.4±0.2
AM7	Lachambre	0.34±0.23		3.9±0.2
AM8	Lachambre	3.59±0.73		6.3±0.7
AM9	Lachambre	0.26±0.18		0.9±0.5
MP2	Mas-Py	2.3±0.44	4.33±2.61	3.6±0.2
MP3	Mas-Py	4.88±0.27		3.1±0.2
MA2-1	Malou-2	2.59±0.61	7.12±0.96	5.2±0.8
GU1	Guano	-	8.13±0.85	0.3±0.0
Si1	Sirach	5.41±1.88	7.6±0.81	5.2±0.6
F1S	Faubourg	3.77±0.7	6.87±2.1	2±0.4
F2S	Faubourg	6.87±1.18	7.13±0.98	7±0.9
F3S	Faubourg	6.38±2.35	6.37±1.12	4.6±1.7
F2A	Faubourg	4.2±0.91		4.5±0.7
F2B	Faubourg	4.69±0.72		5.4±0.5
F2C	Faubourg	2.87±0.36		14.7±2.2
F2D	Faubourg	5.89±2.77		14±1.7
F3	Faubourg	6.98±1.92		6.3±0.4
F4B	Faubourg	3.18±0.67		19.2±2.9
NDVG	Notre-Dame-de-Vie	-	9.03±1.07	0.2±0.0
BA2	Balcon	-	11.88±1.68	0.1±0.0
BA3	Balcon	-	11.78±1.23	0.1±0.0
NID2	Nid	-	11.84±1.93	0.1±0.0
CAM1	Roc Campagna	-	15.92±1.59	0.1±0.0
CAD1	Cady - Canalettes	-		3.5±0.5
CAD1b	Cady - Canalettes	-		5±0.3
CAD2	Cady - Canalettes	-		3.9±0.3
RO1	Rotja - Fulla	-		10.7±1

RO1b	Rotja - Fulla	-		6.8±0.5
RO2	Rotja - Fulla	-		4.5±0.4
TT1	Têt-Thuès	-		4.5±0.3
TT2	Têt-Thuès	-		7.1±0.7
TT3	Têt-Thuès	-		24.1±2.9
TV1	Têt-Villefranche	-		4.5±0.4
TV2	Têt-Villefranche	-		5.6±0.4
TV3	Têt-Villefranche	-		7.2±1.1
EB1	Escaro quarry - base of the formation	1.65±0.95		46.8±5.5
EB2	Escaro quarry - base of the formation	2.63±2.26		70.8±16
EB3	Escaro quarry - base of the formation	3.34±0.95		79.9±9.9
ET1	Escaro quarry - halfway up bench	-		115.4±21.9
ET2	Escaro quarry - halfway up bench	3.4±0.59		30.7±6.4
ET3	Escaro quarry - halfway up bench	2.37±0.71		50.4±5.5

Table 6: Burial durations that were calculated with either the $^{26}Al/^{10}Be$ ratios or the $^{10}Be/^{21}Ne$ ratios and derived maximum paleo-denudation rates. Note that the ^{10}Be concentration is used by default for derived paleodenudation rate calculations.

As suggested by the riverbed samples (Table 6), it is likely that sediments of the Cady and Rotja rivers have experienced a different history from than those of the Têt River, influencing the $^{26}Al/^{10}Be$ ratios measured in the latter. Based on these findings, the favored explanation is that the streams that are draining the Escaro Formation are reworking material that had already been buried. Once trapped in the cave deposits, these sediments increased the variability of the determined $^{26}Al/^{10}Be$ ratios and, therefore, the deduced burial durations and paleo-denudation rates if the sole burial event in the cave was considered.

According to this scenario, sediments that are collected in such cavities may therefore have ^{26}Al and ^{10}Be concentrations (and thus final $^{26}Al/^{10}Be$ ratios) that indicate a burial in the cave that was associated with one pre-burial episode.

Although all the studied caves could present this bias, extrapolating this scenario to the upper stages, whose burial durations are clustered for the Nid and Balcon caves and the dispersion reduced for the Faubourg cave, is more difficult. Moreover, if the burial duration that was determined in this study for the Escaro Formation was proven, the bias that was induced by this pre-buried material would involve only the lowest stages, which probably developed within the same temporal range. Indeed, samples from the Escaro Formation produced burial durations from 2.63 ± 2.26 Ma to 3.40 ± 0.59 Ma (Figure 5; Table 6). Such late Pliocene ages for the deposition of this formation match a hypothesis that was proposed by some authors (Pannekoek, 1935; Oele et al., 1963; Clauzon et al., 2015) but rejected by others (Guitard et al., 1998 and references therein).

Thus, as previously highlighted, the main difficulty from the Têt river valley context is to approximately quantify the effect of the detrital formations on the exhibited records

698　because their quartz grains have experienced multiple burial/exposure cycles. Indeed, some
699　authors (Calvet, 1996 and references therein) reported sufficient thicknesses for these
700　formations to influence all the cavities of the staging. If true, all the analyzed sediments could
701　have had an initial ratio that was more or less different from the expected theoretical
702　production ratio when assuming only one burial event (Laureano et al., 2016). Nonetheless,
703　the clustering of the results for the most perched levels, when sampling several deposits or
704　several caves at the same level was possible, questions the possibility of such an inheritance
705　for these perched levels because of the agreement of the burial durations from both burial
706　dating methods. However, the clustering of their burial durations may have also resulted from
707　a statistical bias. Indeed, few cavities could be studied at high altitudes. Moreover, these
708　cavities exhibited slight development and were small sections, which may not have always
709　been the case because of the morphology of the valley (Figure 2). This finding questions the
710　representativeness of the sampled deposits. Indeed, the retreat of the cliffs could erase
711　morphologies that are essential to the interpretations. In addition, the elevation of the current
712　section may not be representative of the average altitude of the cavities or the altitude of the
713　base levels at the time of their development. It is therefore critical to have the best possible
714　cavity mappings and associated morphological measurements to insure an as accurate as
715　possible altitude location of the selected samples. Finally, only a few remaining deposits are
716　available in the majority of cases, particularly for the most perched levels. Therefore,
717　identifying potential multiple phases of deposition is not guaranteed.

718　　　　Moreover, the age from the measured $^{26}Al/^{10}Be$ ratios of the Escaro Formation (Table
719　6) has geodynamic implications that contradict those from a Lower Burdigalian age (~20 Ma;
720　Baudelot et Crouzel, 1974) based on the occurrence of Lentilla mammal fauna within the
721　same formation and lateral shift in facies (Calvet, 1996 and references therein). Similarly, the
722　thermochronological data from Maurel et al. (2008) suggested a contrasting thermal history
723　that was recorded by two gneiss blocks, with one annealing interpreted as a geothermal effect
724　that occurred during the replay of a fault in the basin ~10 Ma ago. These estimates contradict
725　a Pliocene age based on an apparent continuity and a facies analogy with the Roussillon
726　deposits (e.g., Clauzon et al., 2015 and references therein). To resolve these controversies,
727　investigating other available outcrops near rivers, badlands and mammalian deposits in the
728　Col de Fins and Escaro detrital formations is important to constrain their ages and potentially
729　discard diachronic emplacements.

730　**5.2. Tentative evolution of the Conflent valley since the Burdigalian**
731　**5.2.1. Early and Mid-Miocene evolution of the Têt River valley**

732   Despite all the limitations from the methodological uncertainties, a temporal evolution
733   of the valley can nevertheless be proposed based on the acquired data (Figure 7). The
734   reconstructed "continuous" record of incision evidenced successive stages since the
735   Burdigalian. During the formation of horizontal networks, phases of incision and stagnation
736   must succeed one another (Audra, 1994). Although we cannot accurately constrain when the
737   incision was initiated in the studied area, the results for the Roc Campagna cave enabled us to
738   pinpoint its initiation between 14 and 18 Ma. Several samples were analyzed in the
739   corresponding perched cavities, the burial durations were seemingly clustered from the
740   Burdigalian to the Serravallian. However, only sections of galleries with low development
741   remained, which raises the question of the representativeness of the sampled deposits.
742   Nevertheless, these data from the beginning of the record to approximately 11 - 11.5 Ma
743   produced incision rates from 17 to 21 m/Ma (Figure 7).
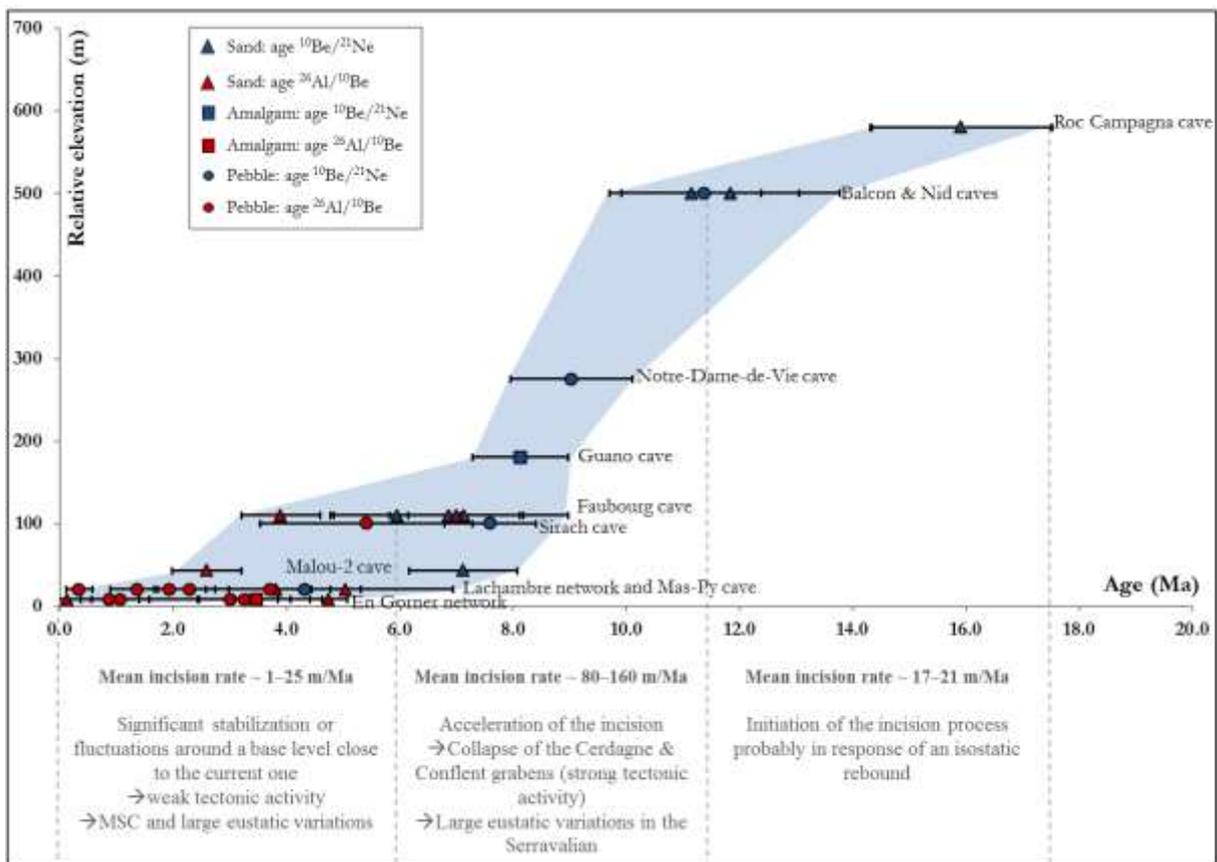
744

745   Figure 7: Evolution of the Têt canyon since the Burdigalian. The deduced burial durations from the
746    $^{26}Al/^{10}Be$ ratios are distinguished from the deduced values from the $^{10}Be/^{21}Ne$ ratios. Incision rates
747   were obtained according to the relative altitudes between two cave entries and the burial durations for
748   these two levels. The small variations in relative altitudes, which were related to gaps in the networks,
749   were included in the uncertainties. The Faubourg and Sirach caves are considered at the same level but
750   on different banks. The same principle was applied to the Lachambre and En Gorner networks. The
751   results for the En Gorner (Puits des Racines), Faubourg and Lachambre networks were not represented
752   (without altering the meaning) to make the graph more readable. "Pebbles" refers to clasts larger than
753   10 cm. "Amalgam" refers to pebble mixing.

754   A significant acceleration of the incision (from x4 to x6) occurred at around 11 - 11.5
755   Ma. This intensification seemed to continue until approximately 6 to 8 Ma ago.

756   The eastern area of the Pyrenees could have been affected by crustal thinning during
757   the 18 – 14 Ma time interval, either after the collision phase or during the last phase of
758   convergence, because of rifting that was linked to the opening of the Gulf of Lion during the
759   Oligo-Miocene (Mauffret et al., 2001). Thenceforth, an uplift episode from an isostatic
760   rebound that was caused by lithospheric thinning in the eastern Pyrenees in response to the
761   opening of the Gulf of Lion and the uplifting of the Canigou massif may have occurred
762   (Maurel et al., 2008). Other hypotheses have been proposed, such as the thermal erosion of
763   the crustal root (Gunnell et al., 2008) or a still-active delamination phenomenon
764   (Vanderhaeghe and Grabkowiak, 2014). Recent geophysical data for the crustal root that were
765   published by Chevrot et al. (2014) did not seem to contradict these assumptions. Therefore, a
766   combination of these phenomena may have been responsible for the initiation of the incision
767   phenomenon, which was mainly linked to an internal forcing.

768   According to Mauffret et al. (2001), a second phase of Late-Miocene extension (ante-
769   Messinian) from 11.5 -11 Ma to ~6 Ma would have caused the formation of the majority of
770   the faults. Additionally, the opening of the grabens of Cerdagne and Conflent occurred from
771   ~12 and ~24 to 6 Ma, respectively (e.g., Guitard et al., 1998). At around the Langhian –
772   Serravallian transition, the global sea level dropped from +90 to -100 m (e.g., Haq et al.,
773   1987). The initiation of the incision acceleration along the record that was reconstructed from
774   this study corresponds to both the opening of the Conflent graben and the drastic Langhian –
775   Serravallian base-level drop. However, can an extensional episode generate incision? The
776   potential creation of relief during this extension episode could have indeed accentuated the
777   incision. .Are internal forcings the only possible explanation? Furthermore, why did we not
778   observe a record that was perturbed by an external forcing, such as base level variations, over
779   this period? Base-level fluctuations were most likely not detectable from the Langhian to the
780   Messinian because of the low proportion of remaining conduits and/or the absence of cavities
781   at the pertinent altimetric range.

782   Finally, if incision from the Burdigalian to the Messinian was caused by both an
783   uprising and variations in the global base level, this could have not been recorded in our
784   dataset because such changes are too subtle in view of the low resolution of the record.
785   Anyway, drawing conclusions regarding the controls of the Miocene incision remains
786   difficult.

787   **5.2.2.   Messinian to present evolution of the Têt River valley**

The deduced burial durations during the recent Miocene were scattered at each sampled cave (Figure 7). As previously presented and discussed, this finding may have resulted from the scattered initial $^{26}Al/^{10}Be$ ratios of the sediments that were deposited within the cavities, which depend on both the pre-burial episode histories and proportion of the Escaro Formation material that was remobilized by the Cady and Rotja rivers and included in the sampled deposits. These rivers specifically contributed to the formation of the Lachambre network and the Ours and Mas-Py caves (right bank of the Têt), which could explain both the scattering of the deduced burial duration in the Lachambre network and the discrepancies between the $^{10}Be/^{21}Ne$ and $^{26}Al/^{10}Be$ burial durations at the Mas-Py cave. However, such dispersions can also be explained by differences in grain sizes (e.g., Codilean et al., 2014), variability in the sources of the catchment, temporary sediment storages (e.g., Wittmann et al., 2011), or stochastic phenomena.

Moreover, global events such as the Messinian Salinity Crisis (MSC, e.g., Clauzon et al., 2015) and the low Pliocene tectonic activity in this area (Delcaillau et al., 2004) may have also been involved in the production of the obtained record, further complicating our interpretations. According to Loget et al. (2005), the MSC caused the fast retreat of the shoreline at the Bourcart canyon (~140 km between 5.6 and 5.46 Ma), which prevented regressive erosion waves from reaching the Têt canyon. The subsequent rise in the overall base level would have been even more intense, probably biphasic, with an episode from 5.46 to 5.33 Ma followed by an almost instantaneous episode whose duration was estimated at 11 years (Pérez-Asensio et al., 2013). Such time intervals would not allow the whole drainage system to amortize these events given the conclusions regarding the migration rate of knickpoints drawn by Loget and Van Den Driessche (2009). A very intense sedimentation phase then occurred in the Roussillon plain, and remnants of Pliocene marine deposits can be observed 7 km from Prades, east of Marquixanes (see Figure 1 for these cities' locations). Furthermore, Molliex et al. (2016) calculated the paleo-denudation rates that affected the Têt sediments, which were 2 to 3 times lower than their and our current rates for the Pliocene sediments. This result can be interpreted as either the result of different climatic conditions that influenced the weathering rate or a reduction in the incision and denudation because of the abrupt rise of the base level. Thus, the incision process in the Conflent could have been modulated by Pliocene eustatism and an aggradation phase may have occurred during the base-level upturns. Finally, the Cerdagne and Conflent faults, similar to those of the Têt, were sealed by the Messinian erosion surface (MES) and were exhumed by denudation processes (Delcaillau et al., 2004). Thus, the tectonic activity likely persisted until the beginning of the Pliocene but did not continue beyond this point. According to this scenario, the near cessation of tectonic activity could explain the overall slowdown in the evolution of the valley.

824 However, some authors have denied this hypothesis (e.g., Briais et al., 1990) because the
825 extension phase continued and these tectonic events were active during the Quaternary. These
826 authors argued that the eustatic control would not have been negligible during this period
827 because of the MSC and subsequent eustatic variations. We cannot currently determine which
828 factors predominantly controlled the incision over this period, so straightforwardly linking
829 incision and uplift rates is impossible.

830 Finally, staggered horizontal galleries that developed during several stages were often
831 linked to the deepening of the valleys. By deduction, the highest level would correspond to
832 the initial position of the river, while the levels close to the river would be contemporaneous
833 with the most recent phases of valley deepening. Although this *per descensum* scheme has
834 long been systematically applied to interpret the staggering of the networks, this scheme has
835 been invalidated in another context (Ardèche) by Mocochain et al. (2009), who proposed an
836 inverse chronology, namely, a *per ascensum* staging of the galleries. This *per ascensum*
837 scenario was based on morphological arguments and, in particular, the peculiar morphology
838 of wells that connected these galleries, which evidenced ascending water circulation in
839 response to base level uprising after the MSC. This type of morphology seems to be absent in
840 the cavities of the Têt canyon (except in the Fuilla-Canalettes network and a well between
841 two galleries in a cave in the Badebany massif), the galleries of which are ample subterranean
842 crossings of the river. This hypothesis thus seems irrelevant in our case to explain the
843 variability of the ratios since the Messinian. However, these observations fall within the
844 current knowledge framework. As already mentioned, we do not know the nature of the
845 networks at the time of their formation because of their subsequent dismantling and/or
846 obstruction.

847 **5.3. Reliability of the derived paleodenudation rates**

848 With the exception of three samples from the lowest stage, namely, the En Gorner's
849 network, which were clasts and not sands, all the samples' concentrations produced maximum
850 paleodenudation rates that were lower than 150 cm/ka (Table 6; Figure 8), similar to those
851 that are characteristic of cratonic zones and to those that were determined in the French
852 Massif Central, which is a component of the Hercynian orogenic belt (Olivetti et al., 2016).
853 Such low maximum paleodenudation rates imply that large initial ^{10}Be, ^{26}Al and ^{21}Ne
854 concentrations accumulated within the quartz minerals of the samples, which in turn implies a
855 long pre-exposure duration at the surface. This finding could support the stability of the
856 massive sources before the initiation of the incision. The maximum paleodenudation rate from
857 the cosmogenic nuclide concentrations in the Roc Campagna alluvium suggests a potential
858 small flat surface that was incised during the Burdigalian. This finding is consistent with the

859 thermochronology data from the Carlit area but not with those from the Canigou and Carança
860 massifs (Maurel et al., 2008).

861   This would mean that the sediments collected in the cavities come from watersheds
862 that have been relatively stable since about 25 Ma, which is not contradictory with the
863 thermochronological data of Maurel et al. (2008) and Gunnell et al. (2009). The presence of
864 Highly-Elevated Low-Relief surfaces can thus partly explain these findings.
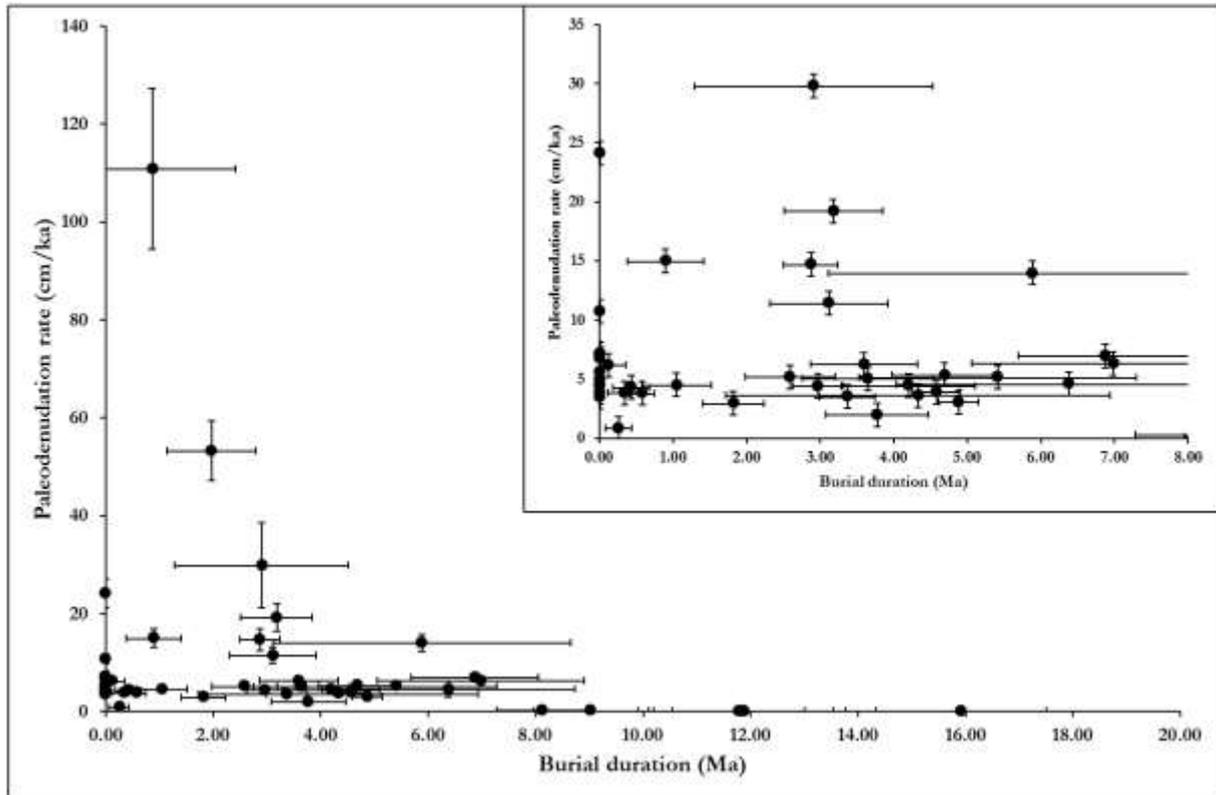
865

866 Figure 8: Paleodenudation rates as a function of time (see Table 6). Most of the data are from the
867 Pliocene to the present. No trend is clearly visible.

868   The thermochronological data acquired for the most part in the west and southwest of
869 the study area document denudations of the order of several hundred meters for the end of the
870 Eo-Oligocene compression period (e.g., Sinclair et al. 2005, Gibson et al., 2007, Jolivet et al.,
871 2007). The thick deposits in the central piedmonts testify to this intense exhumation activity
872 before 30 to 25 Ma, that is during the Eocene and the Oligocene (Poudingues de Palassou in
873 the North and Berga in the South). However, the acquired data do not agree with such high
874 paleodenudation rates and are incompatible with 1 to 2 km thick continental detrital deposits
875 in the Roussillon basin between 23 and 16 Ma. It should also be noted that at least 500 meters
876 thick deposits have been accumulated in the Conflent and Cerdagne basins between 12 and 6
877 Ma (e.g., Calvet, 1996). Such discrepancies have already been observed, but to a lesser extent,
878 by Molliex et al. (2016) who compared the paleodenudation rates derived from the Roussillon
879 basin deposits in the piedmont relative to those derived from continental shelf deposits. They

880 propose that this may result from significantly different time periods over which the
881 denudation processes are integrated. Regarding the ^{10}Be and ^{26}Al cosmogenic nuclides which
882 integrate over several hundred years, the stochastic events are averaged, and are not, or
883 hardly, perceivable in the obtained records. This assertion is all the more true for ^{21}Ne which
884 integrates over a much longer time period and accumulates at each exposure episode.
885 Therefore, although, due to the steady-state assumption, the denudation rates calculated from
886 cosmogenic nuclide concentrations are theoretically maximum denudation rates, they may in
887 fact, due to the occurrence of potential massive stochastic events, be geologically minimum
888 denudation rates.

889   Regarding the significantly higher maximum paleodenudation rates calculated from
890 the concentrations of the En Gorner network samples, no relationship existed between the
891 maximum paleodenudation rates and the particle sizes, so our only possible explanation is the
892 origin of the clasts. Indeed, similar lithologies were found at very remote locations in the
893 watershed. Therefore, we could not discriminate whether the pebbles originated from
894 proximal or distal points in the catchment or whether these rocks were produced in more
895 sloping areas, during particular climatic events, or during stochastic events, among others.
896 Moreover, the high paleo-denudation rates that were determined in this cavity may not be
897 accurate because of potential inheritance of the measured ^{26}Al/^{10}Be ratios at the lower levels
898 from the Escaro Formation.

899   Previous paleodenudation rates from TCN concentrations in the Pyrenees were mainly
900 associated with studies of alluvial terraces in piedmonts (Stange et al., 2012, 2014; Delmas et
901 al., 2015; Nivière et al, 2016; Mouchené et al., 2017), alluvial deposits from large catchments
902 (Molliex et al., 2016), or subglacial and supraglacial ridgetop deposits (Crest et al., 2017).
903 Some preliminary dating of alluvial cave sediments (Genti, 2015) are also available. For the
904 alluvial terraces from the Pleistocene and Holocene, the denudation rates that were derived by
905 these authors were predominantly lower than 20 cm/ka. The rates in the glacial context were
906 also reported to be relatively low, including in the Carlit massif, one of the sources of the
907 studied sediments (Delmas et al., 2009), and river fluvial deposits that were collected from the
908 Têt River watershed produced comparable denudation rates to those in the French Massif
909 Central and the plains (Molliex et al., 2016). Finally, all these published results, which
910 enabled us to distinguish potential paleodenudation gradients between the eastern and western
911 sections of the chain and between the southern and northern piedmonts, are consistent with
912 those in this study.

913 **6. Conclusions**
914

Burial durations from $^{26}Al/^{10}Be$ and/or $^{10}Be/^{21}Ne$ ratios that were measured in alluvial deposits from 11 caves documented a Têt valley incision that occurred in successive stages. The incision likely began during the Early Miocene, probably before 168 Ma, from poorly incised post-orogenic surfaces possibly because of an isostatic rebound that compensated for lithospheric thinning from the opening of the Gulf of Lion. Although we could not determine whether this event was caused by the opening of the Conflent graben and/or a drastic lowering of the global base level around the Langhian – Serravallian transition (~11 Ma), acceleration from ~20 m/Ma to ~80–160 m/Ma of the Têt valley entrenchment was evidenced. The obtained record from the Messinian to the present questioned the methodological assumptions rather than facilitating relatively straightforward geomorphological interpretations and demonstrated the need for a reasoned sampling. This necessity to be cautious regarding the origin and history of the deposits when sampling within cavities (Laureano et al., 2016) is evidenced by both the analyses of riverbed samples and the dating of the Escaro Formation to the Pliocene (at this location). The latter undoubtedly must be further investigated, but this new dataset about this Escaro formation, if true, may have important consequences regarding the global evolution of the massif. This assertion is most likely valid no matter the period (and therefore the level of the karstic system), the relics, or the investigated events, assuming the possible presence of pre-buried material upstream.

Finally, this work demonstrated the scope of the use of cosmogenic ^{21}Ne combined with the determination of ^{10}Be and ^{26}Al concentrations in karstic deposits to determine the abandonment age of karst systems, notably for the oldest systems via the use of the ^{10}Be-^{21}Ne paired nuclides.

Acknowledgments

References

Arnold, M., Merchel, S., Bourles, D.L., Braucher, R., Benedetti, L., Finkel, R.C., Aumaître, G., Gottdang, A., Klein, M., 2010. The French accelerator mass spectrometry facility ASTER: Improved performance and developments. *Nucl. Instr. Methods Phys. Res. B*, 268, 1954–1959. https://doi.org/10.1016/j.nimb.2010.02.107

Audra, P. 1994. Karsts alpins – Genèse de grands réseaux souterrains. *Karstologia Mémoires*, 5. In French

Audra P., Palmer A.N. 2013. The Vertical Dimension of Karst: Controls of Vertical Cave Pattern. *In*: John F. Shroder (Editor-in-chief), Frumkin, A. (Volume Editor) *Treatise on Geomorphology*, Vol 6, *Karst Geomorphology*, San Diego, Academic Press, p. 186-206. https://doi.org/10.1016/B978-0-12-374739-6.00098-1

Babault, J., van den Driessche, J., Bonnet, S., 2005. Origin of the highly elevated Pyrenean peneplain. *Tectonics*, 24, TC2010. https://doi.org/10.1029/2004TC001697

Balco, G., and Shuster, D.L. 2009. ^{26}Al – ^{10}Be – ^{21}Ne burial dating. *Earth and Planetary Science Letters*, 286(3-4), 570-575. https://doi.org/10.1016/j.epsl.2009.07.025

Baudelot, S., Crouzel, F. 1974. La faune burdigalienne des gisements d'Espira-du-Conflent (Pyrénées-Orientales). *Bull. Soc. Hist. Nat. Toulouse*, 110(3–4), 311–326.

Borchers, B., Marrero, S., Balco, G., Caffee, M., Goehring, B., Lifton, N., Nishiizumi, K., Phillips, F., Schaefer, J., and Stone, J. 2016. Geological calibration of spallation production rates in the CRONUS-Earth project. *Quaternary Geochronology*, 31, 188–198. https://doi.org/10.1016/j.quageo.2015.01.009

Bosch, G.V., Van Den Driessche, J., Babault, J., Robert, A., Carballo, A., Le Carlier, C., Loget, N., Prognon, C., Wyns, R. and Baudin, T. 2016. Peneplanation and lithosphere dynamics in the Pyrenees. *Comptes Rendus Geoscience*, 348, 194-202. https://doi.org/10.1016/j.crte.2015.08.005

Braucher, R., Merchel, S., Borgomano, J., Bourlès, D.L., 2011. Production of cosmogenic radionuclides at great depth: a multi element approach. *Earth Planet. Sci. Lett*. 309, 1–9. https://doi.org/10.1016/j.epsl.2011.06.036

Briais, A., Armijo, R.., Winter, T., Tapponnier, P. and Herbecq, A. 1990. Morphological evidence for Quaternary normal faulting and seismic hazard in the eastern Pyrénées. *Annales tectonicae*, IV, 19-42

Brown, E.T., Edmond, J.M., Raisbeck, G.M., Yiou, F., Kurz, M.D., Brook, E.J., 1991, Examination of surface exposure ages of Antarctic moraines using in situ produced [10]Be and [26]Al. *Geochim. Cosmochim. Acta* 55, 2269–2283. https://doi.org/10.1016/0016-7037(91)90103-C

Brown, E.T., Stallard, R.F., Larsen, M.C., Raisbeck, G.M., Yiou, F. 1995. Denudation rates determined from the accumulation of in situ produced [10]Be in the Luquillo Experimental forest, Puerto Rico. *Earth and Planetary Science Letters*. 129, 193-202. https://doi.org/10.1016/0012-821X(94)00249-X

Calvet M. 1996. Morphogenèse d'une montagne méditerranéenne : les Pyrénées orientales. Documents du BRGM, Orléans, n° 255, 3 vol., 1177 p.

Calvet, M., Gunnell, Y., Braucher, R., Hez, G., Bourles, D., Guillou, V., Delmas, M. & ASTER Team. 2015. Cave levels as proxies for measuring post-orogenic uplift: Evidence from cosmogenic dating of alluvium-filled caves in the French Pyrenees. *Geomorphology*, 246, 617-633. https://doi.org/10.1016/j.geomorph.2015.07.013

Chevrot S., Sylvander M., Delouis B. 2011. A preliminary catalog of moment tensors for the Pyrenees. *Tectonophysics*, 510, 239-251. https://doi.org/10.1016/j.tecto.2011.07.011

Chevrot, S., Villaseñor, A. et Sylvander, M. 2014. High resolution imaging of the Pyrenees and Massif Central from the data of the PYROPE and IBERARRAY portable array deployments. *Journal of Geophysical Research*, 119(8), 6399-6420. https://doi.org/10.1002/2014JB010953

Chmeleff, J., von Blanckenburg, F., Kossert, K., Jakob, J, 2010. Determination of the [10]Be half-life by multicollector ICP-MS and liquid scintillation counting. *Nucl. Instr. Methods Phys. Res*. B. 268, 192–199. https://doi.org/10.1016/j.nimb.2009.09.012

Choukroune, P. 1992. Tectonic evolution of the Pyrenees, *Ann. Rev. Earth Planet. Sci*., 20, 143

Clauzon, G. 1982. Le canyon messinien du Rhône : une preuve décisive du « dessicated deep basin model » (Hsü, Cita and Ryan, 1973). Bulletin de la Société Géologique de France, 24, 231-246.

1012 Clauzon, G., Rubino, J.L., Savoye, B. 1995. Marine Pliocene Gilbert-type fan deltas along the
1013 French Mediterranean coast. A typical infill feature of preexisting subaerial Messinian
1014 canyons. IAS-16th egional Meeting of Sedimentology, Field Trip Guide Book, ASF Ed.,
1015 vol.23, Paris, pp. 145-222.

1016 Clauzon, G., Le Strat, P., Duvail, C., Do Couto, D., Suc, J.-P., Molliex, S., Bache, F., Besson,
1017 D., Lindsay, E.H., Opdyke, N.D., Rubino, J.-P., Speranta-Maria Popescu, S.-P., Haq, B.U.
1018 and Gorini, C. 2015. The Roussillon Basin (S. France): A case-study to distinguish local and
1019 regional events between 6 and 3 Ma. *Marine and Petroleum Geology*, 66, 18-40.
1020 https://doi.org/10.1016/j.marpetgeo.2015.03.012

1021 Codilean, A.T., Fenton, C.R., Fabel, D., Bishop, P., Xu, S., 2014. Discordance between
1022 cosmogenic nuclide concentrations in amalgamated sands and individual fluvial pebbles in an
1023 arid zone catchment. *Quaternary Geochronology*, 19, 173-180.
1024 https://doi.org/10.1016/j.quageo.2012.04.007

1025 Debals, B. 2000. Mise au point sur la chronostratigraphie des dépôts alluviaux quaternaires de
1026 la plaine du Roussillon : exemple de la vallée de la Têt (France). *Quaternaire*, 1, 31-39.
1027 https://doi.org/10.3406/quate.2000.1653

1028 Delcaillau, B., Carozza, J.-M. and Font, M. 2004. The northern segment of the Têt Fault
1029 (Pyrenees-Orientales): Neogene evolution and geomorphic implications. *Bulletin de la
1030 Société. Géologique de France*, 175(3), 257-272. https://doi.org/10.2113/175.3.257

1031 Delmas, M., Braucher, R., Gunnell, Y., Guillou, V., Calvet, M., Bourlès, D.L. and ASTER
1032 Team. 2015. Constraints on Pleistocene glaciofluvial terrace age and related soil
1033 chronosequence features from vertical ^{10}Be profiles in the Ariège River catchment (Pyrenees,
1034 France). *Global and Planetary Change*, 132, 39-53.
1035 https://doi.org/10.1016/j.gloplacha.2015.06.011

1036 Depéret, C. 1895. Aperçu de la structure générale et l'histoire de la formation de la vallée du
1037 Rhône. Annales de Géographie, 4, 432-452.

1038 Dunai, T. J. 2010. Cosmogenic Nuclides, Principles, Concepts and Applications in the Earth
1039 Surface Sciences. *Cambridge University Press*, 198 pages; ISBN-13: 9780521873802

1040 Engel, W. 1984. Migration of folding and flysch sedimentation on the southern flank of the
1041 Variscan belt (Montagne Noire, Mouthoumet massif, Pyrenees). *Z. dt. Geol. Ges.*, 135, 279-
1042 292.

Fitzgerald, P.G., Muñoz, J.A., Coney, P.J., Baldwin, S.L. 1999. Asymmetric exhumation across the Pyrenean orogen: implications for the tectonic evolution of a collisional orogen. *Earth and Planetary Science Letters*, 173, 157-170. https://doi.org/10.1016/S0012-821X(99)00225-3

Ford, M., Hemmer, L., Vacherat, A., Gallagher, K and Christophoul, F. 2015. Retro-wedge foreland basin evolution along the ECORS line, eastern Pyrenees, France. *Journal of Geological Society*, 173, 419-437. https://doi.org/10.1144/jgs2015-129

Gautier, F., Clauzon, G., Suc, J.-P., Cravatte, J., Violanti, D. 1994. Âge et durée de la crise de salinité messinienne. Comptes-Rendus de l'Académie des Sciences de Paris, 318(II), 1103-1109.

Genti, M. 2015. Impact des processus de surface sur la déformation actuelle des Pyrénées et des Alpes. Thèse de doctorat, Université de Montpellier, France, 255 pp. In French

Gibson, M., Sinclair, H.D., Lynn, G.J. et Stuart, F.M. 2007. Late- to post-orogenic exhumation of the Central Pyrenees revealed through combined thermochronological data and modeling. *Basin Redearch*, 19, 323-334

Godard, V., Bourlès, D. L., Spinabella, F., Burbank, D. W., Bookhagen, B., Fisher, G. B., Moulin, A. & Léanni, L. 2014. Dominance of tectonics over climate in Himalayan denudation. *Geology*, G35342-1. https://doi.org/10.1130/G35342.1

Granger, D.E., Kirchner, J.W., Finkel, R.C. 1997. Quaternary downcutting rate of the New River, Virginia, measured from differential decay of cosmogenic [26]Al and [10]Be in cave-deposited alluvium. *Geology*, 25, 107–110. . https://doi.org/10.1130/0091-7613(1997) 025<0107:QDROTN>2.3.CO;2

Guitard, G., Laumonier, A., Autran, A., Bandet, Y. and Berger, G.M. 1998. Notice explicative de la carte géologique de Prades (1095) au 1/50000ème. BRGM – Service Géologique National, Ministère de l'Economie, des Finances et de l'Industrie. Editions du BRGM, pp. 198

Gunnell, Y. and Calvet, M. 2006. Comment on « Origin of the highly elevated Pyrenean peneplain », by J. Babault et al. *Tectonics*, 25, TC3003. https://doi.org/10.1029/2004TC001697

Gunnell Y., Zeyen H., Calvet M. 2008. Geophysical evidence of a missing lithospheric root beneath the Eastern Pyrenees: consequences for post-orogenic uplift and associated

geomorphic signatures. *Earth and Planetary Science Letters*, 276, 302-313. https://doi.org/10.1016/j.epsl.2008.09.031

Gunnell, Y., Calvet, M., Brichau, S., Carter, A., Aguilar, J.P. et Zeyen, H. 2009. Low long-term erosion rates in high-energy mountain belts: Insights from thermo- and biochronology in the Eastern Pyrenees. *Earth and Planetary Science Letters*, 278, 208-218

Haq, B.U., Hardenbol, J, Vail, P.R., 1987. Chronology of Fluctuating Sea Levels Since the Triassic. *Science*, 235, 1156-1167. https://doi.org/10.1126/science.235.4793.1156

Häuselmann P., Granger D.E. 2005. Dating of caves by cosmogenic nuclides: method, possibilities, and the Siebenhengste example (Switzerland). *Acta Carsologica*, 34(1), 93-100.

Hez, G. 2015. Un remarquable enregistreur de l'incision de la vallée de la Têt : Le karst étagé des gorges de Villefranche de Conflent Pyrénées-Orientales – France. Mémoire de M2, Université de Savoie Mont-Blanc, 117 pp. In French

Hez, G., Jaillet, S., Calvet, M., and Delannoy, J.-J. 2015. Un enregistreur exceptionnel de l'incision de la vallée de la Têt : le karst de Villefranche-de-Conflent (Pyrénées-Orientales), France. *Karstologia*, 65, 9-32. In French

Honda, M., Zhang, X., Phillips, D., Hamilton, D., Deerberg, M., Schwieters, J.B. 2015. Redetermination of the ^{21}Ne relative abundance of the atmosphere, using a high resolution, multi-collector noble gas mass spectrometer (HELIX-MC Plus). *International Journal of Mass Spectrometry*, 387, 1–7. https://doi.org/10.1016/j.ijms.2015.05.012

Hsü, K.J., Cita, M.B., Ryan, W.B.F. 1973. The origin oft he Mediterranean evaporates. In: Ryan, W.B.F., Hsü, K.J., Cita, M.B., Dumitrica, P., Lort, J.M., Maync, W., Nesteroff, W.D., Pautot, G., Stradner, H., Wezel, F.C., Kaneps, A.G. (Eds), Initial Reports of the Deep Sea Drilling Project, vol.13, U.S. Government Printing Office, Washington, D.C., pp. 1203-1231.

Jolivet, M., Labaume, P., Monié, P., Brunel, M., Arnaud, N. et Campani, M. 2007. Thermochronology constraints for the propagation sequence of the southe Pyrenean basement thrust system (France-Spain). *Tectonics*, 26, TC5007

Keen-Zebert, A., Granger, D.E., Paces, J.B., Hudson, M.R., and Bitting, C. 2016. Combined use of cosmogenic nuclide, U-series disequilibrium, paleomagnetism, and optically stimulated luminescence within Fitton Cave to evaluate the landscape evolution of the Buffalo National River, Arkansas (abs.): *Geological Society of America Abstracts with Programs*, 48(7), doi: 10.1130/abs/2016AM-285655.

1105 Kober, F., Ivy-Ochs, S., Schlunegger, F., Baur, H., Kubik, P.W., Wieler, R. 2007. Denudation
1106 rates and a topography-driven rainfall threshold in northern Chile: Multiple cosmogenic
1107 nuclide data and sediment yield budgets. *Geomorphology*, 83, 97-120.

1108 Korschinek, G., Bergmaier, A., Faestermann, T., Gerstmann, U.C., Knie, K., Rugel,
1109 G.,Wallner, A., Dillmann, I., Dollinger, G., von Gostomski, Lierse Ch., Kossert, K.,
1110 Maitia,M., Poutivtsev, M., Remmert, A., 2010. A new value for the half-life of ^{10}Be by
1111 Heavy-Ion Elastic Recoil Detection and liquid scintillation counting. *Nucl. Instr. Methods*
1112 *Phys. Res. B*, 268, 187–191. https://doi.org/10.1016/j.nimb.2009.09.020

1113 Lagabrielle, Y., Labaume, P. and de Saint Blanquat, M. 2010. Mantle exhumation, crustal
1114 denudation, and gravity tectonics during Cretaceous rifting in the Pyrenean realm (SW
1115 Europe): Insights from the geological setting of the lherzolite bodies. *Tectonics*, 29(4),
1116 TC4012, doi:10.1029/2009TC002588.

1117 Laumonier, B. et coord., 1996. Cambro-Ordovicien, *in Barnolas A., Chiron J.C.: "Synthèse*
1118 *géologique et géophysique des Pyrénées,"* vol. 1, éditions BRGM-ITGE, pp. 157–209.

1119 Laumonier, B. 2015. Les Pyrénées alpines sud-orientales (France, Espagne) – essai de
1120 synthèse. *Rev. Géologie Pyrénéenne*, 2, 1–44.

1121 Laureano, F.V., Karmann, I., Granger, D.E., Auler, A.S., Almeida, R.P., Cruz, F.W., Strícks,
1122 N.M., and Novello, V.F. 2016. Two million years of river and cave aggradation in NE Brazil:
1123 Implications for speleogenesis and landscape evolution. *Geomorphology*, 273, 63-77.
1124 https://doi.org/10.1016/j.geomorph.2016.08.009

1125 Loget, N., van den Driessche, J. and Davy, P., 2005. How did the Messinian salinity crisis
1126 end? *Terra Nova*, 17, 414–419. https://doi.org/10.1111/j.1365-3121.2005.00627.x

1127 Loget, N., Van Den Driessche, J. 2009. Wave train model for knickpoint migration.
1128 *Geomorphology*, 106, 376-382.

1129 Loget, N., Davy, P., van den Driessche, J. 2006. Mesoscale fluvial erosion parameters
1130 deduced from modeling the Mediterranean sea level drop during the Messinian (late
1131 Miocene). *Journal of Geophysical Research*, 111, F03005.
1132 https://doi.org/10.1029/2005JF000387.

1133 Martin, L.C.P, Blard, P.-H., Balco, G., Lavé, J., Delunel, R., Lifton, N., Laurent, V. 2017. The
1134 CREp program and the ICE-D production rate calibration database: A fully parameterizable
1135 and updated online tool to compute cosmic-ray exposure ages. *Quaternary Geochronology*,
1136 38, 25-49. https://doi.org/10.1016/j.quageo.2016.11.006

Mauffret, A., de Grossouvre, B. D., Dos Reis, A. T., Gorini, C., & Nercessian, A. (2001). Structural geometry in the eastern Pyrenees and western Gulf of Lion (Western Mediterranean). *Journal of Structural Geology*, *23*(11), 1701-1726. https://doi.org/10.1016/S0191-8141(01)00025-6

Maurel, O., Monié, P., Pik, R., Arnaud, N., Brunel, M., Jolivet, M. 2008. The Meso-Cenozoic thermo-tectonic evolution of the Eastern Pyrenees: an [40]Ar/[39]Ar fission track and (U–Th)/He thermochronological study of the Canigou and Mont-Louis massifs. *International Journal of Earth Science*, 97, 565–584. https://doi.org/10.1007/s00531-007-0179-x

McPhillips, D., Hoke, G.D., Liu-Zeng, J., Bierman, P.R., Rood, D.H., and Niedermann, S. 2016. Dating the incision of the Yantze River gorge at the First Bend using three-nuclide burial ages. *Geophysical Research Letters*, 43(1), 101-110. https://doi.org/10.1002/2015GL066780

Merchel, S., Herpers, U., 1999. An update on radiochemical separation techniques for the determination of long-lived radionuclides via accelerator mass spectrometry. *Radiochim. Acta* 84, 215–219.

Merchel, S., Bremser, W., 2004. First international 26Al interlaboratory comparison – Part I. *Nuclear Instrumentation Methods in Physics Research, Section B: Beam Interactions with Materials and Atoms*. 223–224, pp. 393–400. https://doi.org/10.1016/j.nimb.2004.04.076

Merchel, S, Arnold, M., Aumaître, G., Benedetti,L., Bourlès, D.L., Braucher, R., Alfimov, V., Freeman, S.P.H.T, and Wallner, A. 2008. Towards more precise [10]Be and [36]Cl data from measurements at the 10^{-14} level: Influence of sample preparation. *Nuclear Instruments and Methods in Physics Research B*, 266, 4921–4926. https://doi.org/10.1016/j.nimb.2008.07.031

Mocochain, L., Audra, P., Clauzon, G., Bellier, O., Bigot, J.-Y., Parize, O., Monteil, P., 2009. The effect of river dynamics induced by the Messinian Salinity Crisis on karst landscape and caves: Example of the Lower Ardèche river (mid Rhône valley). *Geomorphology*, 106, 46-61. https://doi.org/10.1016/j.geomorph.2008.09.021

Molliex, S., Rabineau, M., Leroux, E, Bourlès, D., Authemayou, C., Aslanian, D., Chauvet, F., Civet, F. and Jouët, G. 2016. Multi-approach quantification of denudation rates in the Gulf of Lion source-to-sink system (SE France). *Earth and Planetary Science Letters*, 444, 101-115. https://doi.org/10.1016/j.epsl.2016.03.043

Molnar, P., and England, P. 1990. Late Cenozoic uplift of mountain ranges and global climate change: chicken or egg?, *Nature*, 346, 29-34. https://doi.org/10.1038/346029a0

1169 Monod, B., Regard, V., Carcone, J., Wyns, R. and Christophoul, F. 2016. Postorogenic planar
1170 palaeosurfaces of the central Pyrenees: Weathering and neotectonic records. *Comptes Rendus*
1171 *Geoscience*, 348(3–4), 184–193, doi:10.1016/j.crte.2015.09.005

1172 Mouchené, M., van der Beek, P., Mouthereau, F. and Carcaillet, J. 2017. Controls on
1173 Quaternary incision of the Northern Pyrenean foreland: Chronological and geomorphological
1174 constraints from the Lannemezan megafan, SW France. *Geomorphology*, 281, 78–93,
1175 doi:10.1016/j.geomorph.2016.12.027

1176 Mouchené, M., van der Beek, P., Mouthereau, F., Carcaillet, J. 2017. Controls on Quaternary
1177 incision of the Northern Pyrenean foreland: Chronological and geomorphological constraints
1178 from the Lannemezan megafan, SW France. *Geormophology,* 281, 78-93.
1179 https://doi.org/10.1016/j.geomorph.2016.12.027

1180 Niedermann, S. 2002. Cosmic-ray-produced noble gases in terrestrial rocks: dating tools for
1181 surface processes. *Rev. Mineral. Geochem.* 47, 731-784.
1182 https://doi.org/10.2138/rmg.2002.47.16

1183 Nishiizumi, K.; Imamura, M.; Caffee, M.W.; Southon, J.R.; Finkel, R.C.; McAninch, J. 2007.
1184 Absolute calibration of [10]Be AMS standards. *Nucl. Instrum. Methods Phys. Res. Sect. B*, 258,
1185 403–413. https://doi.org/10.1016/j.nimb.2007.01.297

1186 Nivière, B., Lacan, P., Regard, V., Delmas, M., Calvet, M., Huyghe, D., Roddaz, B., 2016.
1187 Evolution of the Late Pleistocene Aspe River (Western Pyrenees, France). Signature of
1188 climatic events and active tectonics. *Comptes Rendus Geoscience*. doi:
1189 10.1016/j.crte.2015.07.003

1190 Norris, T. L., A. J. Gancarz, D. J. Rokop, and K. W. Thomas (1983), Half-life of [26]Al, *J.*
1191 *Geophys. Res.*, 88(S01), B331–B333, doi:10.1029/JB088iS01p0B331

1192 Oele, E., Sluiter, W.J., and Pannekoek, A.J. 1963. Tertiary and Quaternary sedimentation in
1193 the Conflent, an intramontane rift-valley in the eastern Pyrenees. *Leids geol. Meded*. 28, 297-
1194 319.

1195 Olivetti, V., Godard, V., Bellier, O., ASTER Team. 2016. Cenozoic rejuvenation events of
1196 Massif Central topography (France): Insights from cosmogenic denudation rates and
1197 river profiles. *Earth and Planetary Science Letters*, 444, 179-191.
1198 https://doi.org/10.1016/j.epsl.2016.03.049

1199 Ortuño, M., Martí, A., Martín-Closas, C., Jiménez-Moreno, G., Martinetto, E. and Santanach,
1200 P. 2013. Palaeoenvironments of the Late Miocene Prüedo Basin: implications for the uplift of
1201 the Central Pyrenees. *J. Geol. Soc.*, 170(1), 79–92, doi:10.1144/jgs2011-121

1202 Paces, J.B., Hudson, M.R., Hudson, A.M., Turner, K.J., Bitting, CJ., and Sugano, L.L. 2017.
1203 Isotopic constraints on Middle Pleistocene cave evolution, paleohydrologic flow, and
1204 environmental conditions from Fitton Cave speleothems, Buffalo National River, Arkansas.
1205 (abs.): *In: Kuniansky, E.L., and Spangler, L.E., eds., 2017, U.S. Geological Survey Karst*
1206 *Interest Group Proceedings, San Antonio, Texas, May 16–18, 2017: U.S. Geological Survey*
1207 *Scientific Investigations Report 2017–5023, 245 p.*, http://doi.org/10.3133/sir20175023.

1208 Palmer A.N. 2007. Cave Geology, *Cave Books, Cave Research Foundation*, Dayton, 454 p.

1209 Pannekoek, A.J., 1935. Évolution du bassin de la Têt pendant le Néogène. *Geogr. Geol. Mad.*
1210 *Rijkuniv*. Utrecht 10, p. 72.

1211 Pérez-Asensio, J.N., Aguirre, J., Jiménez-Moreno, G., Schmiedl, G. and Civis J. 2013.
1212 Glacioeustatic control on the origin and cessation of the Messinian salinity crisis. *Global and*
1213 *Planetary Change*, 111, 1-8. https://doi.org/10.1016/j.gloplacha.2013.08.008

1214 Reiners, P.W., Ehlers, T. a, Mitchell, S.G., Montgomery, D.R., 2003. Coupled spatial
1215 variations in precipitation and long-term erosion rates across the Washington Cascades.
1216 *Nature* 426, 645–7. https://doi.org/10.1038/nature02111

1217 Sinclair, H.D., Gibson, M., Naylor, M. et Morris, R.G. 2005. Asymmetric growth of the
1218 Pyrenees revealed through measurement and modeling of orogenic fluxes. *American Journal*
1219 *of Science*, 305, 369-406

1220 Stange, K.M., van Balen, R.T., Kasse, C., Vandenberghe J., Carcaillet, J. 2014. Linking
1221 morphology across glaciofluvial interface: A [10]Be supported chronology of glacier advanced
1222 and terrace formation in the Garonne River, northern Pyrenees, France. *Geomorphology,* 207,
1223 71-95. https://doi.org/10.1016/j.geomorph.2013.10.028

1224 Stange, K.M., van Balen, R.T., Carcaillet, J. & Vandenberghe J. 2013. Terrace staircase
1225 development in the Southern Pyrenees Foreland: Inferences from [10]Be terrace exposure ages
1226 at the Segre River. *Global and Planetary Change*, 101, 97-112.
1227 https://doi.org/10.1016/j.gloplacha.2012.12.007

1228 Stange, K.M., van Balen, R.T., Vandenberghe J., Peña, J.-L. & Sancho, C. 2012. External
1229 controls on Quaternary fluvial incision and terrace formation at the Segre River, Southern
1230 Pyrenees. *Tectonophysics*, 602, 316-331. https://doi.org/10.1016/j.tecto.2012.10.033

Stone, J.O., 2000. Air pressure and cosmogenic isotope production. *Journ. Geophys. Res*. 105, 23753–23759. https://doi.org/10.1029/2000JB900181

Suc, J.-P., Clauzon, G., Cravatte, J., Gautier, F., Violenti, D. 1994. Âge et durée de la crise de salinité messinienne. *Comptes Rendus de l'Académie des Sciences, Paris*, Série II, 318, 1103-1109.

Tassy A., Mocochain L., Bellier O., Braucher R., Gattacceca J., Bourlès D. 2013. Coupling cosmogenic dating and magnetostratigraphy to constrain the chronological evolution of peri-Mediterranean karsts during the Messinian and the Pliocene: Example of Ardèche Valley, Southern France. *Geomorphology*, 189, 81–92. https://doi.org/10.1016/j.geomorph.2013.01.019

Vacherat, A., Mouthereau, F., Pik, R., Bellahsen, N., Gautheron, C., Bernet, M., Daudet, M., Balansa, J., Tibari, B., Jamme, R.P. and Radal, J. 2016. Rift-to-collision transition recorded by tectonothermal evolution of the northern Pyrenees. *Tectonics*, 35(4). https://doi.org/10.1002/2015TC004016

Vanderhaeghe, O. & Grabkowiak, A. 2014. Tectonic accretion and recycling of the continental lithosphere during the Alpine orogeny along the Pyrenees. *Bulletin de la Société Géologique de France*, 185, 143-155. https://doi.org/ 10.2113/gssgfbull.185.4.257

Vergés, J., Fernàndez, M., Martìnez, A. 2002. The Pyrenean orogen: pre-, syn-, and post-collisional evolution. In: Rosenbaum, G., Lister, G. (Eds.), Reconstruction of the Evolution of the Alpine-Himalayan Orogen, Journal of the Virtual Explorer 8. http://dx.doi.org/10.3809/jvirtex.2002.00058.

Vermeesch, P., Balco, G., Blard, P.-H., Dunai, T.J., Kober, F., Niedermann, S., Shuster, D.L., Strasky, S., Finlay, F.M., Wieler, R. & Zimmermann, L. 2012. Interlaboratory comparison of cosmogenic ^{21}Ne in quartz. *Quaternary Geochronology*, 26, 20-28, https://doi.org/10.1016/j.quageo.2012.11.009

Whipple, K.X., 2009. The influence of climate on the tectonic evolution of mountain belts. *Nature Geoscience* 2, 97–104. https://doi.org/10.1038/ngeo413

Wittmann, H., von Blanckenburg, F., Maurice, L., Guyot, J.-L., Kubik, P.W., 2011. Recycling of Amazon floodplain sediment quantified by cosmogenic ^{26}Al and ^{10}Be. *Geology*, v.; no.5; p. 467-470. https://doi.org/10.1130/G31829.1

1261 Zimmermann, L., Avice, G., Blard, P.-H., Marty, B., Füri, E., and Burnard, P.G. Development

1262 of a new full-metal induction furnace for noble gas extraction. *Chemical Geology, under*

1263 *review.*

1264

Supplementary information

1266

Geological and geodynamical contexts

The Conflent geology

1269   The Neogene post-alpine tectonics is very marked in the eastern Pyrenees with the

1270 formation of Neogene to Quaternary narrow intramontane basins (e.g., Conflent, Serdinya,

1271 Capcir) in the Axial Zone. The Conflent basin is delimited by two major N060°E to E-W

1272 Neogene faults: the Têt – Serdinya fault and its eastern relay the Prades fault. The numerous

1273 tectonic markers are often hidden under the Neogene Conflent sedimentary filling.
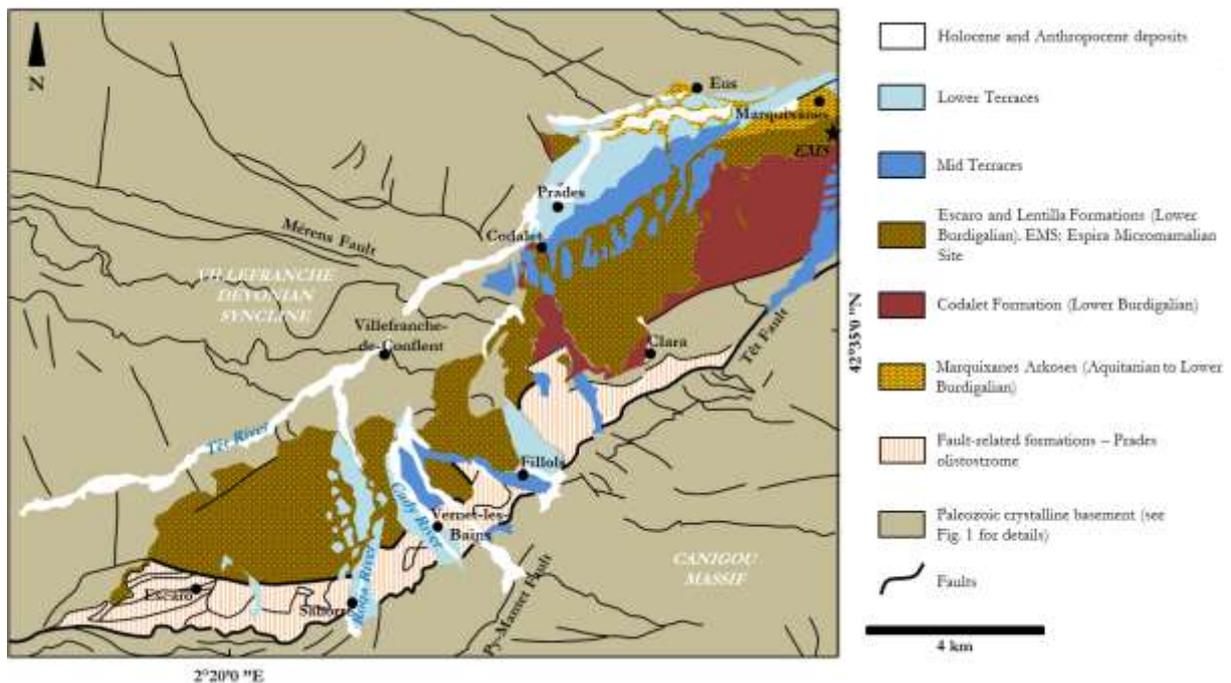
Figure 1: Geological sketch map of the Northwestern Conflent Basin (according to BRGM
data). This map details the various Neogene formations present in the study area. It is
possible to distinguish: the Escaro and Lentilla formations with the Espira micromammalian
site (EMS) of Lower Burdigalian age (Baudelot and Crouzel, 1974), the Codalet Formation of
Aquitanian to Lower Burdigalian age, the Marquixanes Formation of Aquitanian age. Fault-
related formations, including gneiss and micaschist olistoliths, are also present. Finally,
Quaternary formations are represented, without the different levels of terraces being
distinguished in this version.

1283   The base of the filling sequence is dated from the Early Miocene (23-20 Ma), the 200-
1284   500 m thick Marquixanes Formation consisting of arkosic sandstone and granite boulders.
1285   The Lentilla Formation, which overcomes it, has a minimum thickness of 200-400 m. It is
1286   composed of fluviatile facies whose clasts come from the crystalline massifs of Canigou,
1287   Carança and Mont-Louis. Remains of small mammals dated at ~ 20 Ma (Baudelot et Crouzel,
1288   1974) were found at the base of the formation. The Lentilla Formation laterally shifts in facies
1289   to the Codalet Formation which sometimes stratigraphically replaces the Marquixanes
1290   Formation. The Codalet Formation is characterized by its reddish color as well as the
1291   presence of numerous schistous clasts. Moving westward upstream, the Codalet and Lentilla
1292   formations laterally shift to the Escaro Formation, a ~900 m thick sequence constituted by
1293   massive torrential debris. Finally, large olistoliths border the Canigou massif and are
1294   intercalated in the Escaro Formation. This chronology, although generally accepted, is not
1295   unanimous (e.g., Clauzon et al., 2015 and references therein).

Pyrenean highly elevated low-relief surfaces

1297   High-elevation, low-relief surfaces in mountain belts are interpreted as either remnants
1298   of post-tectonic peneplains, which are then used to quantify the uplift of the Earth's surface,
1299   or remnants of peneplains that developed at high elevation because of a progressive rise of the
1300   efficient base level of the drainage system that hampered erosion during the mountain belt
1301   building. These two hypotheses were confronted by Bosch et al. (2016), who proposed that
1302   the elevation of the chain is isostatically compensated at the lithospheric level. The first
1303   hypothesis implying a 2,000-m post-tectonic uprising since the Upper Miocene, these authors
1304   favored the hypothesis of a development of the mid-Miocene Pyrenean peneplain at high
1305   elevation.

1306   Highly elevated low-relief surfaces (HELR; Babault et al., 2005, Calvet and Gunnell,
1307   2008 and references therein for sources of debate), whose ridges reach altitudes as high as
1308   ~2800 m and whose slopes do not exceed 20°, truncate the Paleozoic units of the Pyrenean
1309   range's axial zone and the Mesozoic cover. These surfaces carrying Upper Miocene sediments
1310   in discordance (11.1 – 8.7 Ma) should therefore be anterior to this period.

1311   The origin of these perched surfaces remains enigmatic. It has been proposed that
1312   following an episode of peneplenation, a post-orogenic Pliocene uplift phase would have
1313   occurred. According to De Sitter (1952), this uplift phase would have resulted from tangential
1314   compressive movements that led to crustal thickening of at least 12 km. However, such
1315   movements are not documented. According to Brunet (1986), this phase would have resulted
1316   from the disappearance of all or a portion of the crustal root during the Neogene. However,
1317   geophysical studies (e.g., Chevrot et al., 2014) revealed the presence of a deep root. Thus,

other hypotheses have been developed over the last ten years. Babault et al. (2005) proposed that the HELRs formed at high elevation because of the substantial filling of the foreland basins by the orogen denudation products, which penetrate in discordance back to the chain interior. This scenario involves a general increase in the base level hampering the erosive capacity of the drainage system, as corroborated by analogue modeling (e.g., Babault et al., 2005). However, this hypothesis has been challenged (e.g., Gunnell and Calvet, 2006; Sinclair et al., 2009). Based on geological, thermochronological or geomorphological data, these authors argue that: (i) surface discrimination would be in dispute; (ii) the erosion surfaces would be staggered and at least multiple, with the lowest level at relatively low altitudes and covering large areas and the highest at altitudes between 2700 and 2900 m; (iii) extrapolating the basin fill model is complex; and (iv) the model assumes significant slopes to connect flattened surfaces and clastic sequences of the piedmont. For these last authors, the heavy and dense lithospheric root that was created during the Pyrenean subduction gradually warmed up and disappeared to the east. The vanishing of this thick root of low-density crust that was edified by the Pyrenean tectonics would have then caused a post-orogenic rebound since 10 Ma that led to the current relief. These assumptions regarding the deep structure of the chain have recently been refuted by the acquisition of new data in the framework of national programs (ANR PYROPE, ANR Pyramid). Recent work that considered these data (Bosch et al., 2016) has suggested that the current elevation of the chain is isostatically compensated at the lithospheric level, which contradicts a 2000-m Upper Miocene to Plio-Quaternary uplift of the Pyrenees and implies that peneplains should have developed during the mid-Miocene at high elevation. Thus, uplift knowledge, if any, in this section of the Pyrenees would provide crucial constraints regarding these still-debated hypotheses.

References

Babault, J., van den Driessche, J., Bonnet, S., 2005. Origin of the highly elevated Pyrenean peneplain. *Tectonics*, 24, TC2010. https://doi.org/10.1029/2004TC001697

Baudelot, S., Crouzel, F. 1974. La faune burdigalienne des gisements d'Espira-du-Conflent (Pyrénées-Orientales). *Bull. Soc. Hist. Nat. Toulouse*, 110(3–4), 311–326.

Bosch, G.V., Van Den Driessche, J., Babault, J., Robert, A., Carballo, A., Le Carlier, C., Loget, N., Prognon, C., Wyns, R. and Baudin, T. 2016. Peneplanation and lithosphere dynamics in the Pyrenees. *Comptes Rendus Geoscience*, 348, 194-202. https://doi.org/10.1016/j.crte.2015.08.005

Brunet, M.F. 1986. The influence of the evolution of Pyrenees on adjacent basins. *Tectonophysics*, 129, 343-354. https://doi.org/10.1016/0040-1951(86)90260-X

Calvet M., Gunnell Y. 2008. Planar landforms as markers of denudation chronology: an inversion of East Pyrenean tectonics based on landscape and sedimentary basin analysis. *In: Gallagher K., Jones S.J., Wainwright J. (eds), Landscape Evolution: Denudation, Climate and Tectonics Over Different Time and Space Scales, Geological Society, London, Special Publications*, 296, 147–166. https://doi.org/10.1144/SP296.10

Chevrot, S., Villaseñor, A. et Sylvander, M. 2014. High resolution imaging of the Pyrenees and Massif Central from the data of the PYROPE and IBERARRAY portable array deployments. *Journal of Geophysical Research*, 119(8), 6399-6420. https://doi.org/10.1002/2014JB010953

Clauzon, G., Le Strat, P., Duvail, C., Do Couto, D., Suc, J.-P., Molliex, S., Bache, F., Besson, D., Lindsay, E.H., Opdyke, N.D., Rubino, J.-P., Speranta-Maria Popescu, S.-P., Haq, B.U. and Gorini, C. 2015. The Roussillon Basin (S. France): A case-study to distinguish local and regional events between 6 and 3 Ma. *Marine and Petroleum Geology*, 66, 18-40. https://doi.org/10.1016/j.marpetgeo.2015.03.012

De Sitter, L.U. 1952. Pliocene uplift of Tertiary mountain chains. *American Journal of Science*, 250, 297-307. https://doi.org/10.2475/ajs.250.4.297

Gunnell, Y. and Calvet, M. 2006. Comment on « Origin of the highly elevated Pyrenean peneplain », by J. Babault et al. *Tectonics*, 25, TC3003. https://doi.org/10.1029/2004TC001697

Sinclair, H.D., Gibson, M., Lynn, G., and Stuart, F.M. 2009. The evidence for a Pyrenean Resurrection: a response to Babault *et al*. (2008). *Basin Research*, 21, 143-145. https://doi.org/10.1111/j.1365-2117.2008.00391.x